

Lasse Svendsen Chrobak

Characterization of Coke Formation in The direct Synthesis of Dimethyldichlorosilane

In collaboration with Elkem - Bluestar

Masteroppgave i Chemical Engineering and Biotechnology

Veileder: Hilde J. Venvik

Medveileder: Mehdi Mahmoodinia

Juni 2021

Lasse Svendsen Chrobak

Characterization of Coke Formation in The direct Synthesis of Dimethyldichlorosilane

In collaboration with Elkem - Bluestar

Masteroppgave i Chemical Engineering and Biotechnology
Veileder: Hilde J. Venvik
Medveileder: Mehdi Mahmoodinia
Juni 2021

Norges teknisk-naturvitenskapelige universitet



Kunnskap for en bedre verden

Abstract

The direct synthesis of dimethyldichlorosilane has been used in the silicone industry for over 60 years. Even though the process is the most convenient and economical way to produce dimethyldichlorosilane, the process mechanism is still debated today. This is due to the complexity of the reaction as a three-phase reaction. Gaseous methyl chloride reacts with the contact mass, a mixture of silicon powder, copper catalyst and chosen promoters. Side reactions during the direct process result in catalyst deactivation in the form of coke formation. Coke formation is a significant issue but is not well understood.

This thesis work has analyzed a series of contact mass samples with different reaction times and promotion of tin or co-promotion of tin and zinc. These samples were characterized using Auger electron spectroscopy (AES) and Fourier-transform infrared spectroscopy (FT-IR) to investigate the structural order of the coke and temperature-programmed oxidation (TPO) to study the coke reactivity. AES depth profiling was used to investigate the coke deposition layer and its connection to other elements.

AES investigation of the characteristic carbon peak (C(KLL)) showed that reacted contact mass samples contain coke deposition with amorphous and graphitic structure. No difference in coke morphology was found for samples with and without Zn promotion. Coke morphology was found to become more graphitic with increasing reaction time.

AES depth profiling showed that reacted contact mass samples were mostly homogeneous Cu or Si beneath the surface layer. Coke deposition layers were mostly found on Cu-containing particles. Depth profiling showed high heterogeneity within the contact mass samples.

TCD results from TPO revealed peaks attributed to combustion of coke at $\sim 270^{\circ}\text{C}$ and $\sim 380^{\circ}\text{C}$, with some variance. No trends were found for these TCD peaks. Another TCD peak appearing straight after the coke combustion was attributed to oxidation of the newly exposed surface. Contact mass reacted for 16 hours and 40 hours had significantly more exposed surface than contact mass reacted for 5 hours.

FT-IR results showed signals attributed to highly unsaturated coke. This peak was not present for samples with a reaction time of 5 hours, but clearly visible at 16 hours and 40 hours reaction time. This was concluded to coke amount increasing with reaction time.

Sammendrag

Den direkte syntesen av dimetyldiklorsilan har blitt brukt i silikonindustrien i over 60 år. Selv om prosessen er den mest praktiske og økonomiske måten å produsere dimetyldiklorsilan, så er prosessmekanismen fremdeles omstridt. Dette er på grunn av reaksjonens kompleksitet som en tre-fase reaksjon. Metylklorid i gassform reagerer med kontaktmassen, en blanding av silisumpulver, kobberkatalysator og promotorer. Sidereaksjoner under den direkte syntesen fører til deaktivering i form av koksdannelse. Koksdannelsen er et betydelig problem for prosessen, men er ikke godt forstått.

Denne oppgaven har analysert flere kontaktmasseprøver med forskjellige reaksjonstider og promotering med tinn eller co-promotering med tinn og sink. Disse prøvene ble karakterisert ved hjelp av Auger elektron spektroskopi (AES) og Fourier-transformasjon infrarød spektroskopi (FT-IR) for å undersøke den strukturelle orden til koksdannelsen, og temperaturprogramert oksidasjon (TPO) for å se på reaktiviteten til koksen. AES dybdeprofilering ble brukt til å undersøke laget av koksdannelse og dens sammenheng til andre elementer.

AES undersøkelser av den karakteristiske karbontoppen (C(KLL)) viste at reagerte kontaktmasseprøver inneholder koksdannelse med amorf og grafittisk struktur. Ingen forskjeller i morfologien til koks ble funnet for prøver med og uten Zn promotering. Undersøkelse av morfologien til koks viste at strukturen ble mere grafittisk med økende reaksjonstid.

AES dybdeprofilering viste at reagert kontaktmasse for det meste består av homegent Cu eller Si under overflaten. Kokslag ble for det meste funnet på partikler bestående av hovedsakelig Cu. Dypdeprofilering viste høy heterogenitet innad i kontaktmasseprøvene.

TCD resultater fra TPO hadde topper attributtet til forbrenning av koks ved $\sim 270^{\circ}\text{C}$ and $\sim 380^{\circ}\text{C}$, med litt varierende temperaturer. Ingen trend ble funnet for disse toppene. En annen TCD topp synlig rett etter forbrenningen av koks ble koblet til oksidering av nylig eksponert overflate. Kontaktmasse reagert i 16 timer og 40 timer hadde betydelig mer eksponert overflate enn kontaktmasse reagert i 5 timer.

FT-IR resultater viste signaler attributtet til umettet koks. Denne toppen var ikke tilstede for prøver med reaksjonstid på 5 timer, men synlig for prøver med 16 timer og 40 timer reaksjonstid. Dette ble konkludert til at koksmengden øker med reaksjonstid.

Preface

This Master's thesis has been done under the Department of Chemical Engineering at the Norwegian University of Science and Technology (NTNU), in collaboration with Elkem Silicone Materials. The thesis is a part of the two-year master's degree program Chemical Engineering and Biotechnology. The thesis was accomplished under the supervision of Professor Hilde J. Venvik and co-supervision of Dr. Mehdi Mahmoodinia at the Department of Chemical Engineering at NTNU, Trondheim.

Acknowledgment

I would like to thank my supervisor Hilde J. Venvik for providing valuable guidance and help throughout the two semesters. The weekly discussions and feedback has been immensely helpful. I express my sincere gratitude to my co-supervisor Dr. Mehdi Mahmoodinia for his continuous guidance and feedback. My appreciation also extends to Torbjørn Røe from Elkem Silicone Materials and the rest of the people in the HECSI project meetings for helpful feedback and discussions. I would also like to thank senior engineer Estelle M. Vanhaecke for providing technical training and support for the laboratory work.

Trondheim, Norway 27.06.21



Lasse Svendsen Chrobak

Table of Contents

Abstract	i
Sammendrag	i
Preface	iii
Table of Contents	vi
List of Tables	vii
List of Figures	x
Abbreviations	xi
1 Introduction	1
1.1 Scope of the Thesis	2
2 Theory	3
2.1 The Direct Synthesis	3
2.1.1 Mechanism of the Direct Synthesis	4
2.1.2 CuCl as the Copper Catalyst	4
2.1.3 Role of the Active Phase	5
2.1.4 Role of Promoters	6
2.1.5 Deactivation by Coke Formation	7
2.2 Characterization Techniques	9
2.2.1 Scanning Electron Microscopy	9

2.2.2	Auger Electron Spectroscopy	9
2.2.3	Depth profiling	11
2.2.4	Temperature-Programmed Oxidation	11
2.2.5	Fourier Transform Infrared Spectroscopy	12
3	Materials and Methods	15
3.1	Reference and Contact Mass Samples	15
3.2	Auger Electron Spectroscopy and Scanning Electron Microscopy	16
3.3	Fourier Transform Infrared Spectroscopy	18
3.4	Temperature-Programmed Oxidation	19
4	Results and Discussion	21
4.1	AES study of Coke Chemistry	21
4.2	Depth Profiling on Carbon Containing Particles	24
4.2.1	Heterogeneity of Reacted Contact Mass - AES	30
4.3	TPO Analysis	31
4.3.1	TCD Results	31
4.3.2	TCD Results for Reacted Contact Mass	32
4.3.3	MS Results from TPO Analysis	35
4.4	FT-IR Investigation of Reacted Contact Mass	37
5	Conclusion	43
6	Future Work	45
	References	47
	Appendix	57
A	Additional FT-IR Figures	57
B	Additional TPO Figures	58
C	Full TPO Procedure	60
D	Risk Assessment	63

List of Tables

3.1	Shows an summarized explanation of the analyzed samples CuCl, reference silicon, unreacted contact mass and the reacted contact mass samples.	16
3.2	Description of AES modes, including their energy resolution, sensitivity and purpose.	17
3.3	Overview of elements, their peak assignment, kinetic energy interval (eV) and sensitivity factor used for AES depth profile quantification. All information was provided in the JEOL AES software.	18
3.4	Thermal conductivity for gases relevant to TPO analysis at 400 K [52].	19
4.1	Summary of FT-IR peaks detected for the reacted contact mass samples. The approximate peak value (wavenumber), the designated bond and sources backing the designation is shown.	38

List of Figures

2.1	Illustration of the direct synthesis reaction and the distribution of all the products. [4].	4
2.2	Energy spectrum of a sample irradiated with primary electrons. Contributions come from inelastic processes (secondary electrons), primary electrons, plasmon losses, and loss electrons. Auger electrons will produce specific element peaks on top of an intense background. The Auger peaks are therefore more visible in derivative spectra [32].	10
2.3	Optical diagram of an interferometer [49].	13
3.1	Principle diagram cross-section of the JAMP-9500F setup [51].	17
4.1	Figure (a) shows plotted C(KLL) peaks in the kinetic energy range of 234-292 eV for all reacted contact mass samples. All intensities were normalized to better compare the line shape. (b) shows plotted standard spectra of the C (KLL) peak for SiC and graphite. These standards were provided with the JEOL AES software.	22
4.2	SEM images (SEI, x3000) from depth profile analysis of the S18 sample. Before (a), and after sputtering (b) for 20000 s or an approximate sputtering depth of 10 μ m. . . .	24

4.3	Depth profiles for different reacted contact mass samples. All profiles were sputtered with 120 s cycles and M5 settings. An approximate depth scale is shown in all depth profiles.	28
4.4	TCD signal versus temperature for all contact mass samples. The signals were offset along the y-axis for clarity.	32
4.5	CO_2 MS signal ($m/z=44$) and temperature versus time during TPO experiment for all reacted contact mass samples except S20.	36
4.6	FT-IR results of all reacted contact mass samples in the full wavenumber region of $600-4000\text{ cm}^{-1}$. The equipment was purged with N_2 gas for to minimize the effect of atmospheric moisture and CO_2 and increase the intensity of IR radiations. All spectra have been baseline corrected.	37
4.7	FT-IR results of all reacted contact mass samples in the high wavenumber region, $3000-4000\text{ cm}^{-1}$. The equipment was purged with N_2 gas to minimize the effect of atmospheric moisture and CO_2 and increase the intensity of IR radiations. All spectra have been baseline corrected.	39
4.8	FT-IR results of all reacted contact mass samples in the high wavenumber region, $600-1700\text{ cm}^{-1}$. The equipment was purged with N_2 gas to minimize the effect of atmospheric moisture and CO_2 and increase the intensity of IR radiations. All spectra have been baseline corrected.	41
A.1	FT-IR results of all reacted contact mass samples in the high wavenumber region, $3000-4000\text{ cm}^{-1}$. The reacted contact mass samples have been exposed to air, and not purged with N_2 . All spectra have been baseline corrected. These FT-IR spectra were collected without N_2 purging.	57
B.2	CO_2 TCD signal and temperature versus time during TPO experiment for two S20 parallels.	58
B.3	CO_2 MS signal ($m/z=44$) and temperature versus time during TPO experiment for all reacted contact mass samples.	59
C.4	Detailed settings for TPO procedure step 1, pretreatment.	60
C.5	Detailed settings for TPO procedure step 2, TPO.	61
C.6	Detailed settings for TPO procedure step 3, posttreatment.	62

Abbreviations

AES	=	Auger Electron Spectroscopy
ATR	=	Attenuated Total Reflection
a.u.	=	Arbitrary Units
EDX	=	Energy Dispersive X-ray Spectroscopy
FT-IR	=	Fourier Transform Infrared Spectroscopy
IR	=	Infrared
H/C	=	Hydrogen to Carbon Ratio
M2	=	Dimethyldichlorosilane
MS	=	Mass Spectrometer
NTNU	=	Norwegian University of Science and Technology
SEI	=	Secondary Electron Imaging
SEM	=	Scanning Electron Microscopy
S(T)EM	=	Scanning (Transmission) Electron Spectroscopy
TCD	=	Thermal Conductivity detector
TGA	=	Thermogravimetric Analysis
TPO	=	Temperature Programmed Oxidation
TPR	=	Temperature Programmed Reduction
URCM	=	Unreacted Contact Mass
XPS	=	X-ray Photoelectron Spectroscopy
XRD	=	X-Ray Diffraction

Introduction

In 1939 Eugene Rochow discovered a way to synthesize methylchlorosilanes using a copper catalyst [1]. This breakthrough formed the basis of modern silicone industry. All previously attempted processes were not industrially feasible. Richard Müller was researching the synthesis of $HSiCl_3$ and discovered the direct synthesis of methylchlorosilanes independently in the early 1940s, sometime after Rochow [2]. The process called the Rochow-Müller process or the direct synthesis is the most common process to produce methylchlorosilanes, which is the starting material for producing silicone polymers [3]. The direct synthesis is to this day regarded as the most convenient and economical process for producing silicone monomers. 90% of all starting materials for silicone production are made through the direct synthesis [4].

Silicone products, mostly resins and elastomers, are used in many different applications due to their unique properties [5]. Silicone products are used for thermal and electrical insulators due to their thermal aging resistance [4]. Chemical resistance is another property of silicones and is needed for sealants in the construction industry [6]. Several other applications are found in the medical, textile and food industry, to name a few [2].

The direct synthesis is a complex, three-phase, heterogeneous catalytic process [4]. A blend of silicon powder, copper catalyst and promoters is mixed and referred to as contact mass. The contact mass reacts with gaseous methyl chloride (CH_3Cl) in a "gas-solid-solid" three phase reaction and forms a complex range of monomeric methylchlorosilanes [5]. Dimethyldichlorosilane (M2), is the most desirable product for use in the

silicone industry and is industrially obtained with high selectivity, around 85 % [1]. Side reactions during the direct process result in catalyst deactivation in the form of coke deposition. The direct process comes to a halt before all the silicon is consumed due to deactivation by coke formation on the surface [7]. This makes it necessary to remove spent contact mass from the reactor and replace it to maintain constant production. Even though the coke formation is a significant issue, the process has not received much attention and is not well understood [3].

1.1 Scope of the Thesis

The aim of this thesis is to further develop a methodology to help understand the mechanism behind coke formation. To understand the mechanism behind the formation of coke, it is important to understand the type of coke. Hence, relevant characterization techniques are applied to investigate the coke composition and structural order. One aim of the thesis is to find a correlation between coke amount, coke composition, contact mass promotion and reaction progress. Unreacted contact mass and different reacted contact mass samples are analyzed by using different characterization techniques. Contact mass samples with different reaction times with or without Zn promotion are investigated for trends. The gathered results are discussed in connection with previously reported research.

Theory

2.1 The Direct Synthesis

The direct synthesis of methyl methylchlorosilanes, also called the Rochow-Müller process is the most common way to produce methylchlorosilanes. The synthesis is a reaction between methyl chloride (CH_3Cl) and silicon which is catalyzed by copper. The reaction yields a wide range of products as shown in Figure 2.1, which makes it quite complex [3].

The direct synthesis is a unique three-phase, "gas-solid-solid" reaction [3]. The solids, silicon powder, copper catalyst and promoters, are mixed and called contact mass. The contact mass is reacted with CH_3Cl at temperatures between 290 and 330°C [4, 5]. The most desired product is dimethyldichlorosilane ($(CH_3)_2SiCl_2$, M2), although many other methylchlorosilanes are produced. The ideal reaction for M2 production is shown in Equation 2.1 [4, 8].



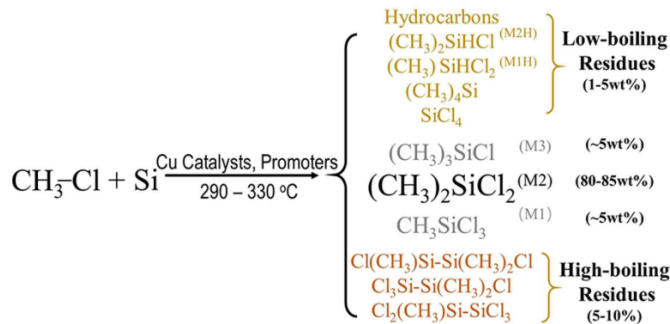


Figure 2.1: Illustration of the direct synthesis reaction and the distribution of all the products. [4].

2.1.1 Mechanism of the Direct Synthesis

The direct synthesis has been industrially viable since it was disclosed, but knowledge of the catalytic reaction mechanism is still meager. There are many reasons for this, mainly a large number of reaction variables: Silicon impurities, catalyst properties, usage of promoters, and the high complexity of the reaction [9]. The wide product distribution and yields will vary with the catalyst and promoters, catalyst preparation, and reaction temperature and pressure. Other parameters as product residence time, catalyst heterogeneity, promoter distribution, and many more make the direct synthesis a highly complex system [7].

Another factor that complicates and differentiated the direct synthesis from other catalytic reaction is that Si acts as both reactant and catalyst. An alloy intermediate is formed between Cu and Si. The mechanism is still debatable today, but a Cu-Si alloy, Cu_3Si , is generally claimed to be the catalytic active component [4, 9]

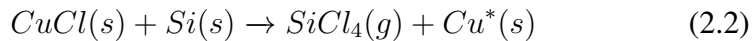
2.1.2 CuCl as the Copper Catalyst

The direct synthesis became possible when copper was discovered as a catalytic material for the reaction. Without a catalyst the CH_3Cl and Si behave practically inert to each other [1, 8]. Several different Cu-based compounds have been used as the catalytic material for the direct synthesis. These can be referred to as "coppers" and are e.g. CuCl, CuCl₂, CuO, elemental Cu, and Cu₂O. Cu is usually referred to as the catalyst in the direct synthe-

sis, but this is not a correct term [4]. A catalyst is by definition a material that changes the reaction rates and directions without being consumed itself [10]. The correct definition for Cu is catalyst precursor since Cu reacts into the active phase (Cu_3Si) that is generally considered to be the catalytic component. Cu is however still referred to as the catalyst for the direct synthesis by most researchers [4].

Although many different copper catalysts can be used, CuCl is often referred to as the model catalyst. CuCl is ideal for research purposes since it has a brief induction period [4]. The induction period is defined as the time period during which active catalytic surface for methylchlorosilanes is formed [11, 12, 13]. There are initially no silanes being formed during the induction period, instead there is formation of methane, hydrogen and carbon [5]. In addition to the advantages of using CuCl, it has several disadvantages. CuCl by itself is very unstable and can absorb water or oxidize [4]. Another disadvantage is that the use of CuCl increases the amount of byproducts in the form of $SiCl_4$.

When using CuCl, active Cu is formed during the induction period as shown in Equation 2.2 where contact mass is heated to the reaction temperature [14].



This produces activated Cu, denoted with an asterisk, but also the byproduct $SiCl_4$. Activated Cu will then react with Si to form several alloys as discussed later in Section 2.1.3 [14].

Chen et al. reported that CuCl morphology affects the reaction. It was reported that dendritic CuCl with regular morphology and exposed (111), (200), and (220) planes showed much higher M2 selectivity and Si conversion compared to commercial CuCl microparticles [15].

Acker et al. studied the difference between industrial-bought pyrolytic CuCl and CuCl prepared by wet chemical method. It was reported that wet process CuCl exhibits higher reactivity towards Si [16].

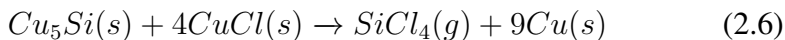
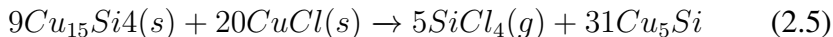
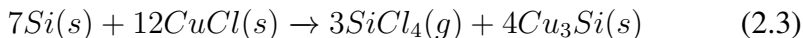
2.1.3 Role of the Active Phase

Most investigations agree that Cu_3Si is the active Cu-Si phase for the direct synthesis [4]. Cu_3Si , also called η -phase is an intermetallic alloy formed when Si reacts with activated Cu [17]. Si in newly formed Cu_3Si is con-

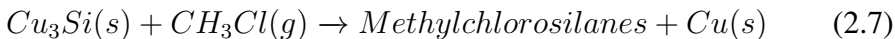
tinuously consumed while activated Cu diffuses into the bulk Si to form more Cu_3Si [17, 18]. Frank et al. reported that Cu_3Si provides an active surface for selective formation of M2 [19]. Cu increases the M2 selectivity by increasing the M2 formation while suppressing the formation of other methylchlorosilanes [19].

Another Cu-Si alloy has been reported to be present in the direct synthesis; $Cu_{15}Si_4$, called the ϵ -phase. Luo et al. reported that $Cu_{15}Si_4$ formation depends on the particle size of CuCl, and the cause for $Cu_{15}Si_4$ formation is agglomeration of CuCl. $Cu_{15}Si_4$ acts as a "copper reservoir" since formation of $Cu_{15}Si_4$ decreases the reactivity due to necessary decomposition of $Cu_{15}Si_4$ into Cu_3Si [9].

Weber et al. suggested that the decomposition of $Cu_{15}Si_4$ to Cu_3Si and further to Cu happens according to Equation 2.3, 2.4, 2.5 and 2.6. Equation 2.3 also covers the reaction for formation of the Cu_3Si phase [20].



Cu_3Si and $Cu_{15}Si_4$ can also decompose and reverse the reaction when there is formed low Cu/Si ratio intermetallic compounds. Cu_3Si will also decompose in direct synthesis conditions as shown in Equation 2.7 [9].



2.1.4 Role of Promoters

Copper is to this day the best catalyst for the direct synthesis, although it lacks sufficient selectivity and activity by itself [21]. To achieve a more acceptable selectivity towards M2, one needs to use promoters [4]. Promoters are materials that enhance the performance of the catalyst by co-adding it

to the catalyst [10]. The promoters themselves usually have no catalytic activity [20]. There are several known promoters for the direct synthesis; Zinc (Zn), tin (Sn), and several others [4]. These promoters have been empirically optimized for industrial use. The functionality of these promoters are not well understood due to the complexity of the direct synthesis [21]. Some of the known promoters are unintentionally introduced to the system through Si impurities. The main impurities in Si particles are Fe, Al and Ca [14, 21]. Al has been reported to increase reaction activity and shorten the induction period [4]. Presence of Al also results in higher Zn vapor pressure and increased ability to transfer Zn to reaction sites [22].

Zn is often regarded as the most efficient promoter for the direct synthesis [21]. Zn is found to enhance the formation of the Cu_3Si -phase when co-added with CuCl [23]. Potochnik and Falconer found that subsurface Si concentration in the Cu_3Si alloy increases when promoting with Zn [24]. Zn can also accelerate the formation of $Si - CH_3$ bonds. This is done by increased adsorption of CH_3Cl as Zn acts as a methylating agent [23].

Sn has been reported to have a big synergistic effect when co-promoted with Zn. Promoting with both Zn and Sn can reduce the surface tension and melting point of Cu_3Si . This increases the surface transfer of Cl and accelerates the formation of active $SiCl_x$ [25, 26]. Sn is also an effective promoter by itself. Sn promotion can increase the concentration of surface methyl species [25]. Sn promoted CuCl can have an accelerated consumption of Cu_3Si [21].

2.1.5 Deactivation by Coke Formation

Catalyst deactivation, described as the loss of activity and/or selectivity, is a major problem in catalytic processes. Both chemical and mechanical deactivation occurs simultaneously with the main reaction, and is inevitable for most processes. Deactivation is usually divided into four categories, poisoning, fouling, sintering, and phase formation [27].

Coke formation is a specific type of fouling. Fouling is the deposition of species onto the catalytic surface. The deactivation happens due to blocking of active surface [28].

Catalytic generation of coke or carbon is a significant deactivation reaction for processes with the presence of CO, methane, or other hydrocarbons. Coke and carbon are terms that are mostly interchangeable since the difference is somewhat arbitrary [5]. Carbon is typically produced from CO

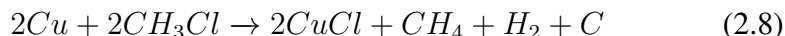
disproportionation, while coke is produced from decomposition or condensation of hydrocarbon. Therefore, the phenomenon is later referred to as coke formation [28].

Reaction conditions are very important for coke formation. It affects the molecular structure, macroscopic structure, and reactivity of the coke deposition [29]. The reaction temperature is often the most important condition for the composition of coke formation. For low temperature reaction, $<200^{\circ}\text{C}$, the coke is usually not polyaromatic, while coke formation with temperature over 350°C mainly yields polyaromatic compounds. The coke composition also heavily depends on the active site of the catalyst, as the nature of the active site (acid, base, metal etc.) determine the type of catalyzed reaction step [30].

Despite the significant deactivation coke formation causes the catalyst in the direct synthesis, the mechanism is not understood. The only certain aspect is that side reactions during the process lead to the formation of the carbonaceous residue [3]. In a fluidized bed reactor, the direct process comes to a halt before all the silicon is consumed due to the deactivation of the active phase by coke deposition and enrichment of inactive copper on the surface [7].

It was proposed by Bažant that the coke is formed from decomposition of methyl radicals and is comprised of polymethylenes [31].

Clarke however claimed that the coke is formed from methyl chloride cracking on copper. The cracking can be empirically described by Equation 2.8 [8].



Luo et al. reported no presence of coke from XRD analysis and concluded that the carbonaceous residue is amorphous. It was also reported that the amount of coke depends on the Cu quantity. This supports the theory that coke formation hinders diffusion of Cu [9].

Wessel and Rethwisch reported two types of coke formation for the direct synthesis, α -coke and β -coke. It was reported a loss of activity from β -coke forming on top of the catalytic sites. Formation of α -coke does not affect the catalytic activity. They also reported that α -coke contains a higher hydrogen to carbon (H/C) ratio than β -coke. Formation of β -coke was also enhanced at higher reaction temperatures [3].

2.2 Characterization Techniques

This section presents characterization techniques used to investigate the contact mass samples and coke deposition.

2.2.1 Scanning Electron Microscopy

Scanning electron microscopy (SEM) is a microscopic technique that can yield imaging with resolution down to 10 nm [32]. SEM imaging can show information on particle size, shape, composition, crystallography, and other chemical or physical properties of the sample [33].

The principle of SEM is based on a finely focused beam of energetic electrons emitted from an electron source. The electron beam is emitted from the source and modified by different apertures, lenses, and electromagnetic coils. This successively reduces the beam radius that scans the sample on closely spaced locations in a raster pattern. The interaction between the sample and electron beam produces two electron responses: Backscattered electrons and secondary electrons [33]. Secondary electron imaging (SEI) gives information on the topography and the geometric nature of the sample, while backscattered electrons give information on the compositional structure of the sample [32].

2.2.2 Auger Electron Spectroscopy

Auger electron spectroscopy (AES) is a widely used characterization technique for analyzing chemical properties and composition on surfaces [34]. The technique is very sensitive and has a typical detection limit of 0.1 at%. During an AES experiment, a focused beam of primary electrons irradiate the sample. The primary electrons will then penetrate the sample in the depth of 0.1 to 1 μm depending on the energy of the primary electrons. This results in ionization of different electron orbitals in the sample. Electrons from other shells can then fill up the ionized states. Energy is released from this process into either a photon in the form of X-ray emission or transmitted to another electron in the outer orbitals and emitted from the atom as an Auger electron [35].

AES is based on the Auger process. The Auger process involves ionization of an atom following deexcitation when an electron from the outer orbitals decays to fill the ionized state. The excess energy generated by this

will then cause an other electron, an Auger electron, to be emitted. When the Auger process happens on the surface, the Auger electrons can leave the surface without energy loss and give a signal in the secondary electron distribution. The composition of the surface can be identified using Auger transitions that are unique for each element [36].

When plotting AES spectra, one usually uses the derivative mode of the energy distribution, $dN(E)/dE$. This is because the Auger electron intensity is small and superimposed on a large background of inelastically scattered electrons[32, 37, 38]. The energy spectrum will have contributions from secondary electrons at lower kinetic energy and from plasmon loss, loss electrons and primary electrons at higher kinetic energies[32]. This effect is shown graphically in Figure 2.2. Peak-to-peak signal strength of the derivative spectra is also used as a relative quantitative measure of elemental surface concentration [37, 38].

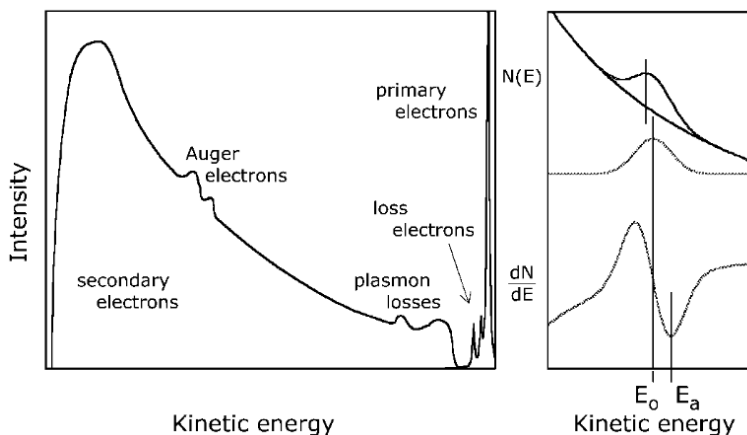


Figure 2.2: Energy spectrum of a sample irradiated with primary electrons. Contributions come from inelastic processes (secondary electrons), primary electrons, plasmon losses, and loss electrons. Auger electrons will produce specific element peaks on top of an intense background. The Auger peaks are therefore more visible in derivative spectra [32].

AES is a surface analysis technique that can measure every element, except hydrogen and helium, simultaneously. Another property of AES is the ability to determine the chemical valence of elements and distinguish between chemical species. Chemical valence, electronegativity difference, and the radius of ion in compounds all affect the so called chemical shift.

[39].

Environment changes of an atom on the surface can change the Auger electron spectra in several ways such as shift in the energy where Auger peaks occur and changed in the shape of a group of overlapping Auger peaks [40, 41]. AES instruments are often fitted with SEM for the purpose of sample positioning [32].

2.2.3 Depth profiling

Depth profiling is a quantitative surface analysis technique that obtains the depth-dependent composition of the sample. AES or X-ray photoelectron spectroscopy (XPS) in combination with sputtering is the most used type of depth profiling [35].

In depth profiling, sputtering is the bombardment of the sample surface with energetic primary particles, often argon ions (Ar^+). The sputtering causes erosion by emission of secondary particles from the sample and exposes deeper surface layers [42]. Sputtering is alternated with surface analysis to make a quantitative depth profiling. The sputtering process is complex and can significantly modify the structure and composition of the analyzed surface layer. One example is if the incident ion energy is too low to transfer the energy equivalent of the surface binding, the atom will remain bound and not sputtered [43].

2.2.4 Temperature-Programmed Oxidation

Temperature-programmed oxidation (TPO) is a characterization method where oxidation of the sample is monitored while the temperature increases. The instrumentation for TPO and other temperature-programmed reaction methods is quite simple. A reactor containing the sample is heated at a set rate, while oxidant (usually O_2) flows through the reactor. A thermal conductivity detector (TCD) or mass spectrometer (MS) measures the composition of the outlet gas[10].

When using O_2 as the oxidant, it is consumed from the gas mixture, which is then detected by the TCD. The change in TCD signal will increase proportionally to the rate of oxygen consumption. The maximum of the peak will represent the highest rate of oxidation. Several oxidation products as H_2O , CO and CO_2 can be formed during TPO and will interfere with the TCD signal [44].

The carrier gas for TPO is usually 5% O_2 in He, to optimize the thermal conductivity difference between reactant gas and carrier gas. sample gas. TCD is also a detector that is concentration sensitive and will not change the sample gas, as it is nondestructive [32, 45].

Temperature-programmed techniques are the most widely used techniques to study the reactivity and thermal behavior of coke. TPO with oxygen diluted with inert gases is usually used. TPO experiments often include detection with TCD or MS to detect and quantify CO_2 in the outlet gas[46].

2.2.5 Fourier Transform Infrared Spectroscopy

Fourier transform infrared spectroscopy(FT-IR) is a spectroscopic technique based on the principle that molecular vibrations absorb infrared radiation in the range of electromagnetic radiation. Infrared (IR) radiation is electromagnetic radiation in frequencies between 14300 and 20 cm^{-1} . The mid-IR region, 4000 to 400 cm^{-1} , is the most used range for analyzing organic materials since most molecular groups have vibration energies in this range [47].

The principle behind FT-IR is that each vibration has a unique frequency that depends on the mass of atoms and the strength of the chemical bond between them. The IR spectrum is obtained from IR passing through a sample and analyzing what fraction of the incident radiation is absorbed at a specific energy. This specific energy corresponds to a frequency of a vibration of a sample molecule [47].

FT-IR spectroscopy uses an interferometer for IR measurement. An interferometer consists of two plan mirrors and a beam splitter as shown in Figure 2.3 [48, 49]. The IR radiation from the source hits the beamsplitter and is separated. One IR beam goes through the beamsplitter to the fixed mirror, and the other IR beam is reflected from the beam splitter towards the moving mirror. Both mirrors reflects the IR radiation back to the beam splitter and create an interference pattern called an interferogram. This interferogram is measured by a detector and transformed into a spectrum by the Fourier transform algorithm [47].

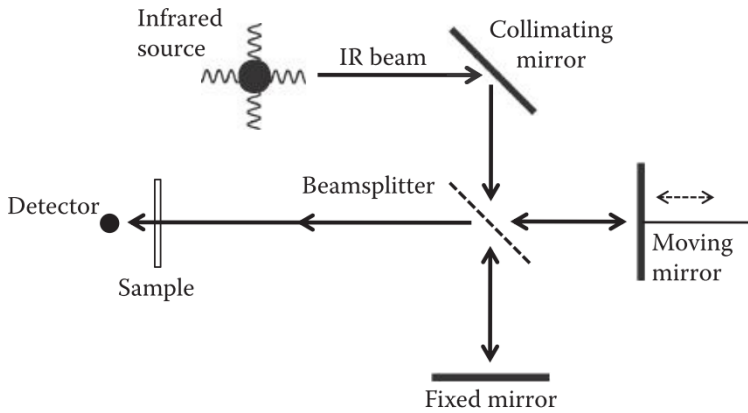


Figure 2.3: Optical diagram of an interferometer [49].

The Fourier transform can calculate the superposition of sine and cosine waves for a given function. An interferogram is a superposition of cosine waves. Therefore an Fourier transform of an interferogram obtains a function that corresponds to the interferogram [49].

Attenuated total reflectance (ATR) is a sampling technique used in FT-IR spectroscopy. The infrared beam travels from an ATR crystal with a high refractive index to the sample with a low refractive index. This will reflect part of the light back to the low refraction index sample. At a specific angle of incident, most of the light is reflected back, this is called total internal reflection. Some of the light energy will escape the crystal and extend beyond the surface. The reflected light intensity reduces at this point. This is a phenomenon called attenuated total reflectance. Some of the radiation that extends beyond the crystal is absorbed by the sample. The absorbed radiation is translated into the IR spectrum of the sample [50].

Materials and Methods

A risk assessment for all methods used in this thesis was carried out and is attached in Appendix D. The key risk factor for the thesis work is prolonged exposure to powder samples and its unknown health risk.

3.1 Reference and Contact Mass Samples

All samples analyzed in this master's thesis were provided by Elkem Silicon Materials. The unreacted contact mass (URCM) contains a standard amount of CuCl, and standard promotion of Zn and Sn. Reacted contact mass samples was reacted in a fluidized bed reactor for the specified amount of time. The reactor was operated at 4 bar and 300°C. CH_3Cl and Ar gas were feed with a flow of 295 mL/min and 10 mL/min, respectively. The reactor was run as semi-batch, with a continuous feed of CH_3Cl , but no addition of contact mass.

The reacted contact mass samples S13 and S14 have a reaction time of 5 hours. S13 contains five times the normal amount of CuCl and both promoters, Zn and Sn. S14 contains five times the amount of CuCl and Sn promoter. Sample S17 and S18 have a reaction time of 16 hours and. S17 contains five times the normal amount of CuCl and both promoters, Zn and Sn. S18 contains five times the amount of CuCl and Sn promoter. Both S19 and S20 have a reaction time of 40 hours and contains five times the normal amount of CuCl and Sn. In addition, S19 contains five times the amount of Zn.

The overview of the analyzed samples is summarized in Table 3.1. Classification of reacted contact mass samples is based on reaction time and relative amount of CuCl, Zn, and Sn.

Table 3.1: Shows an summarized explanation of the analyzed samples CuCl, reference silicon, unreacted contact mass and the reacted contact mass samples.

Sample	Explanation	CuCl amount	Zn amount	Sn amount
Si-Ref	MG silicon	-	-	-
URCM	S0-URCM	Standard	Standard	Standard
S13	S13-Si5(CuZnSn)-5h	5 times	5 times	5 times
S14	S14-Si5(CuSn)-5h	5 times	-	5 times
S17	S17-Si5(CuZnSn)-16h	5 times	5 times	5 times
S18	S18-Si5(CuSn)-16h	5 times	-	5 times
S19	S19-Si5(CuZnSn)-40h	5 times	5 times	5 times
S20	S20-Si5(CuSn)-40h	5 times	-	5 times

MG: Metallurgical grade, URCM: Unreacted contact mass

3.2 Auger Electron Spectroscopy and Scanning Electron Microscopy

JEOL JAMP-9500F was used to perform SEM imaging and AES depth profiling. Figure 3.1 shows a principle diagram of the instrument setup. Contact mass samples were mounted on sample holders using carbon tape. SEM images were obtained using an accelerating voltage of 10.0 kV. AES energy resolution and sensitivity settings were determined by presets as described in Table 3.2. The M5 mode was used for all depth profiling experiments to achieve the highest elemental sensitivity. Depth profiling was achieved by Ar⁺ sputtering with a probe current of 9 nA, ion current of $3.3 \cdot 10^{-6}$ A, and beam energy of 3000 eV. The samples' subsurface region was analyzed by alternating sputtering and AES analysis with 120 s sputtering intervals. The sample surface was sputtered for up to 10000 or 20000 s for different particles.

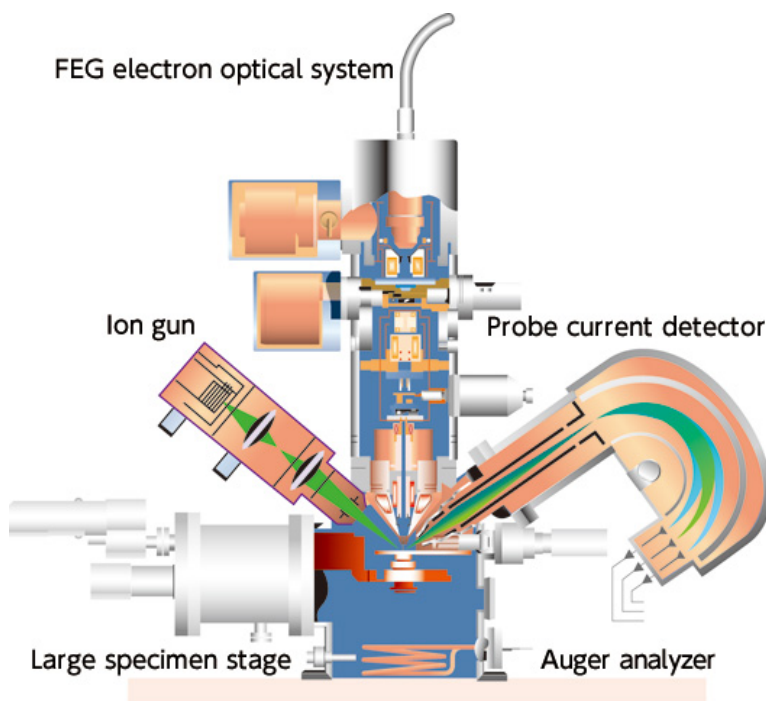


Figure 3.1: Principle diagram cross-section of the JAMP-9500F setup [51].

Table 3.2: Description of AES modes, including their energy resolution, sensitivity and purpose.

Mode	Energy Resolution	Sensitivity	Purpose
M5	0.5 %	High	Qualitative, quantitative analysis
M4	0.35 %	Middle	Quantitative, chemical state analysis
M3	0.15 %	Low	Chemical state analysis
M2	0.05 %	Low	Energy loss spectrum

All AES data were processed in CasaXPS to achieve differentiated spectra. Differentiation was achieved using the Savitzky–Golay quadratic method with a varying smoothing width based on the signal noise.

Depth profile quantification was carried out in CasaXPS based on differentiated peak-to-peak amplitudes. Specific sensitivity values for each

element, provided in the JEOL AES software, were used for elemental weighting. These sensitivity values are specific for an accelerating voltage of 10 kV. Elemental peaks, respective kinetic energy intervals, and sensitivity factors are shown in Table 3.3. The Si (KLL) peak is chosen over Si (LVV) for quantification. The Si (LVV) peak is more surface sensitive than the Si (KLL) peak, but its line shape and intensity are sensitive to the silicon chemical environment [24].

Table 3.3: Overview of elements, their peak assignment, kinetic energy interval (eV) and sensitivity factor used for AES depth profile quantification. All information was provided in the JEOL AES software.

Element	Peak	Energy interval (eV)	Sensitivity factor
Cl	LVV	169 - 193	1.505
C	KLL	234 - 292	0.121
O	KLL	481 - 526	0.365
Cu	LMM	899 - 929	0.556
Zn	LMM	971 - 1002	0.515
Al	KLL	1375 - 1405	0.340
Si	KLL	1588 - 1640	0.238

3.3 Fourier Transform Infrared Spectroscopy

FT-IR was carried out using Bruker Tensor 27 FT-IR spectrometer with a diamond crystal (MKII Golden Gate™, Speccac) single reflection ATR-cell with the Opus 4.2 software. All FT-IR spectra were collected with a resolution of 4 cm⁻¹, 64 scans. All data were collected in the 600-4000 cm⁻¹ range. Baseline correction was carried out in the OPUS 4.2 software. For some experiments, the equipment was purged with N₂ gas for 72 hours prior to analysis to minimize the effect of atmospheric moisture and CO₂ and increase the intensity of IR radiations. Samples were installed by covering the crystal with the powder sample, and tightening the anvil on top. FT-IR experiment with N₂ purging was performed by Hammad Farooq.

3.4 Temperature-Programmed Oxidation

TPO experiments were carried out on a BenchCAT Hybrid 1000 HP instrument with AMI Control Software. The instrument was coupled with TCD and MS detectors. Analysis was carried out with 50 mL/min 5% O₂/He carrier gas. The temperature profile was set with a heating rate of 10°C/min to a maximum temperature of 700°C. A treatment step was carried out before and after the oxidation step. An overview of all the steps in the procedure and detailed settings is shown in Appendix C. An overview of thermal conductivity for relevant gases is found in Table 3.4 [52]. Each sample was prepared in a quartz u-tube. The samples (~150 mg) were placed in a catalyst bed between quartz wool layers.

Table 3.4: Thermal conductivity for gases relevant to TPO analysis at 400 K [52].

Element	Thermal conductivity (at 400 K) [mW/mK]
<i>He</i>	189.6
<i>Ar</i>	22.4
<i>O₂</i>	34.0
<i>CO₂</i>	24.7
<i>CO</i>	31.7
<i>H₂O</i>	26.4

Results and Discussion

4.1 AES study of Coke Chemistry

Figure 4.1 shows the characteristic AES carbon peak (KLL) within the kinetic energy range of 234 to 292 eV [38]. All reacted contact mass samples (S13, S14, S17, S18, S19 and S20) are shown in Figure 4.1a. The spectra are shown in the derivative form ($dN(E)/dE$) and the intensity is normalized to compare the peak line shape. AES data for the carbon peaks was taken after 720s of sputtering to avoid adventitious carbon.

Figure 4.1b shows standardized spectra for silicon carbide(SiC) and graphite obtained from the JEOL AES software. As seen in Figure 4.1b, the main difference in the line shape is the two positive peaks at ~ 250 eV and ~ 265 eV. SiC AES standard shows a peak at ~ 265 eV, but no peak at ~ 250 eV. The standard graphite spectrum shows a clear and proficient peak at ~ 250 eV, while the peak at ~ 265 eV is barely deviating from the baseline shape. Lurie and Wilson analyzed a standard line shape for amorphous carbon. The amorphous carbon showed a broad peak at ~ 250 eV with a slope reaching out to ~ 265 eV. Amorphous carbon showed a loss in the fine structure in the signal from AES [53].

The C(KLL) spectra for the reacted contact mass samples show no line shapes that correspond completely to one carbon type. The characteristic area to focus on is between 240 and 270 eV. None of the samples shows a peak at ~ 250 eV but no proficient peak at all at ~ 265 eV, Because of this it is safe to say that the carbon is not present as SiC.

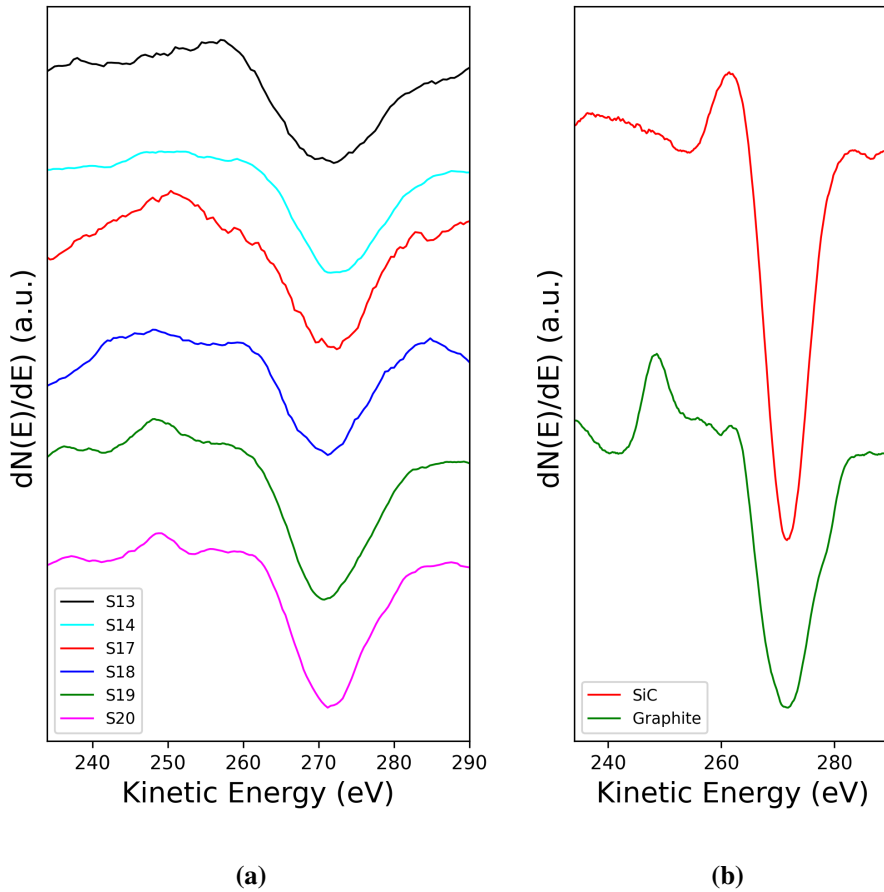


Figure 4.1: Figure (a) shows plotted C(KLL) peaks in the kinetic energy range of 234-292 eV for all reacted contact mass samples. All intensities were normalized to better compare the line shape. (b) shows plotted standard spectra of the C (KLL) peak for SiC and graphite. These standards were provided with the JEOL AES software.

Samples reacted for 5 hours (S13 and S14) show a somewhat flat line shape. S13 shows a small peak at 265 eV, while S14 shows a generally flat profile. After 16 hours (S17 and S18) the line shape looks more defined for both samples showing a visible peak at 250 eV. The line shape of S17 shows no clear shoulder between the peaks, and exhibits a line shape similar

to amorphous carbon. Unlike S17, the S18 sample exhibit a clear shoulder between the peaks, which can mean a more graphitic structure.

Samples that have been reacted for 40 hours (S19 and S20) show a very similar line shape. Both samples have a proficient peak at 250 eV and a clear shoulder between the peaks. This suggests that the coke deposited on the sample after 40 hours of reaction shows a more graphitic structure. All of this suggests that the coke morphology becomes more graphitic with increasing reaction time.

4.2 Depth Profiling on Carbon Containing Particles

Figure 4.3 shows AES depth profiles of reacted contact mass samples. The atomic concentration is plotted against sputtering time. All elemental atomic concentrations (C, Cl, O, Cu, Zn, and Si) were estimated using differentiated peak-to-peak amplitudes with sensitivity factors from JEOL. The Cl(LVV), C(KLL), O(KLL), Cu(LMM), Zn(LMM), Al(KLL), Si(KLL) peaks were used. All peaks, energy intervals, and sensitivity factors are shown in Table 3.3. Depth approximation is based on the sputtering rate of 29.3 nm/min for SiO_2 (value shown in the JEOL AES software). As sputtering is preferential towards different elements, the approximation only valid within the same order of magnitude [35].

Figure 4.2 shows an example of SEM images with x3000 magnification from before and after AES depth profiling. The S18 sample was sputtered for 20000 s or an approximate depth of 10 μm . The AES data was taken from a spot in the middle of the SEM area. The images show the relatively large area affected by the sputtering.

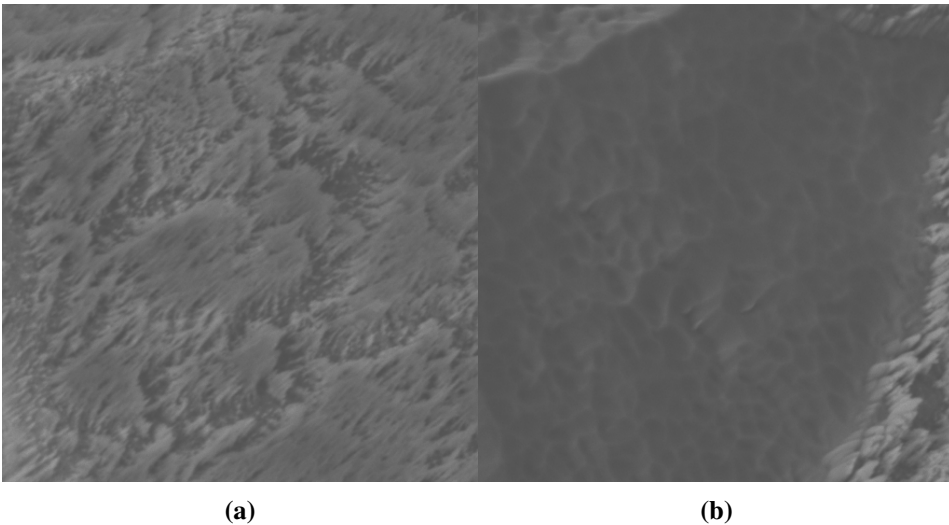
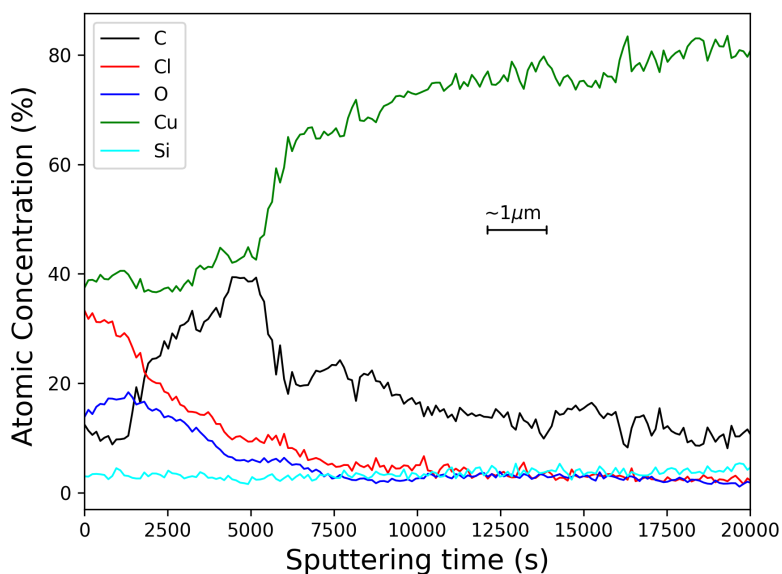
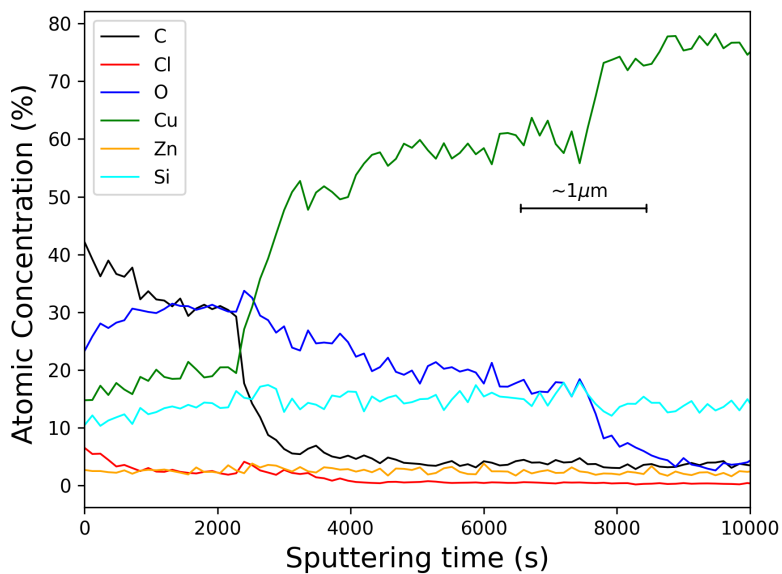


Figure 4.2: SEM images (SEI, x3000) from depth profile analysis of the S18 sample. Before (a), and after sputtering (b) for 20000 s or an approximate sputtering depth of 10 μm .

The aim of the AES depth profiling experiments was to analyze coke deposition layers on all the reacted contact mass samples. This was quite comprehensive due to the heterogeneity of the sample (discussed in Section 4.2.1) and was not accomplished. The depth profiles presented are therefore only for some of the samples, and not reproduced for all.

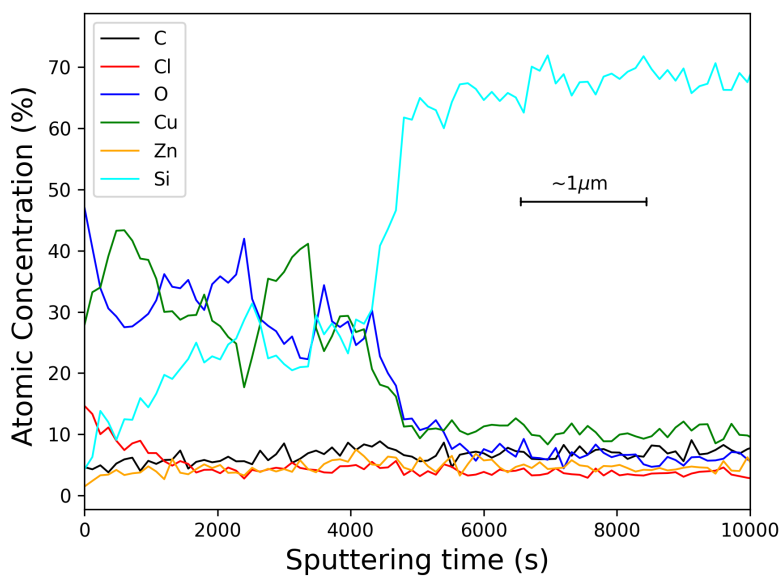


(a) AES composition versus sputtering time for an S20 particle.

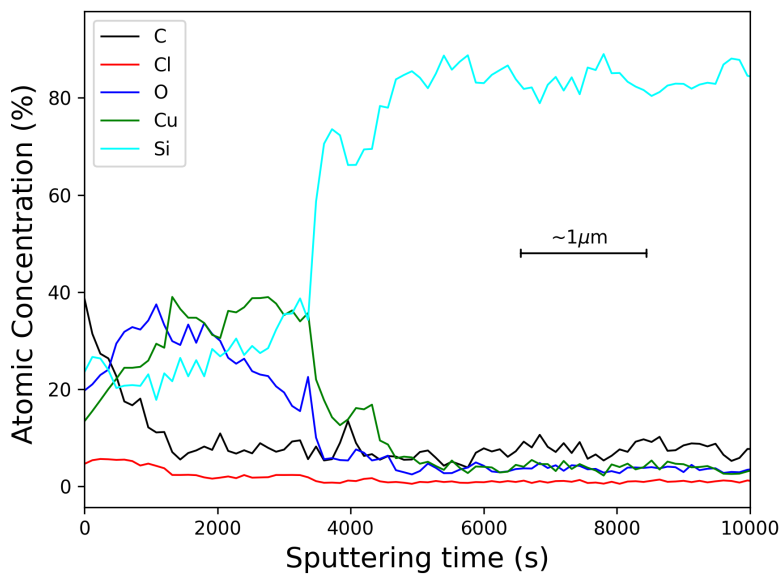


(b) AES composition versus sputtering time for an S19 particle.

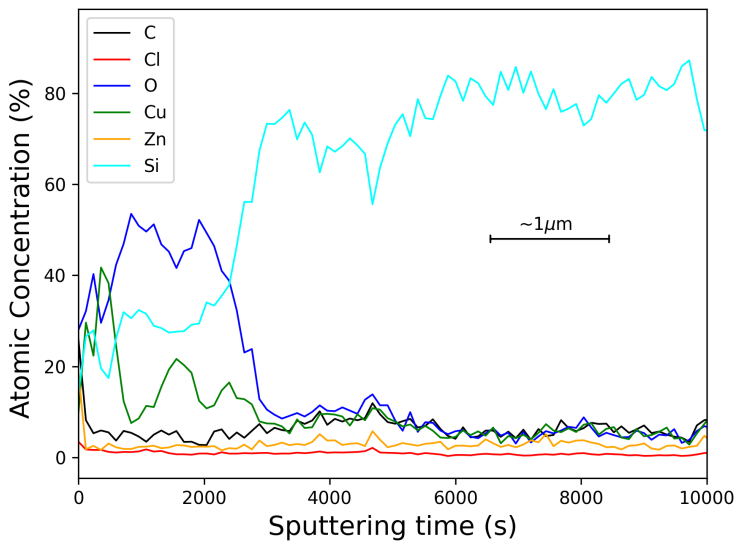
4.2 Depth Profiling on Carbon Containing Particles



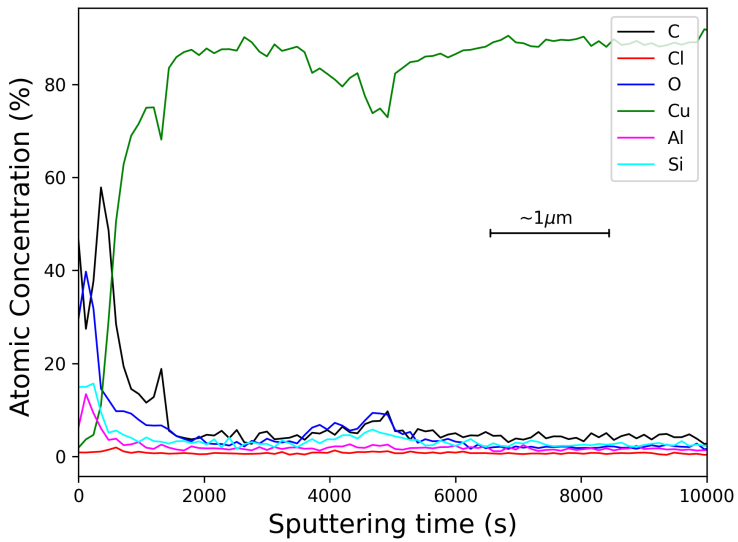
(c) AES composition versus sputtering time for an S19 particle.



(d) AES composition versus sputtering time for an S18 particle.



(e) AES composition versus sputtering time for an S17 particle.



(f) AES composition versus sputtering time for an S14 particle.

Figure 4.3: Depth profiles for different reacted contact mass samples. All profiles were sputtered with 120 s cycles and M5 settings. An approximate depth scale is shown in all depth profiles.

Figure 4.3a shows a depth profile from the S20 sample. This profile shows a mostly Cu-containing particle, with a carbon layer that drops but remains at a lower concentration throughout the whole profile. The constant presence of carbon during the end of the depth profile might be due to the analysis spot hitting a surface edge with coke deposition instead of sputtering through a flat deposition layer. Cl is present in a relative large quantity on the surface that constantly decreases until no Cl is detected. Cl may be present as CuCl from used Cl reacting with deactivated Cu. O is also detected and is most likely present as an oxide layer from exposure to air.

Figure 4.3b shows a depth profile from sample S19. The profile shows a clear carbon layer on the particle. The presence of O signal is somewhat constant, then suddenly drops. This suggests an oxide layer, attributed to the sample reacting in air during sample transfer. The increasing Cu signal suggests that the particle is mostly Cu beneath the surface layer. A constant Si presence is seen on the sample, this may mean that Si is present in the form of a Cu-Si alloy.

Figure 4.3f shows a depth profile for the S14 sample. The analyzed particle seems to be a Cu particle with a carbon deposition layer. O, Si and Al are also detected on the surface, but not further into the particle. Al was seen for only two scans on the surface and was not detected in any other depth profiles. The amount of Al was low, corresponding to it originating from impurities in Si powder[9]. The low concentration of Al and the small detection area of the AES makes Al hard to detect and is why it was not seen in any other depth profile.

Figure 4.3c shows another depth profile on the S19 sample. This particle is mostly Si beneath a surface layer of Cu and O. This suggests that copper oxide is present on the surface. The concentration of Si before sputtering is zero, which suggests that the copper oxide layer completely covers the Si particle. The depth profile of an S17 particle shown in Figure 4.3e, pictures a similar Si particle. A copper oxide layer covers the surface, with a mostly Si particle beneath the surface. Carbon is detected in the initial AES scan before sputtering, which can be attributed to adventitious carbon.

Figure 4.3d shows another depth profile on a Si particle, from sample S18. This profile share similarities with Figure 4.3c and 4.3e, such as low start concentration of Si and a copper oxide layer. This sample, however, has a thin carbon layer at the surface.

The presence of the coke layer on the Cu particle suggests that coke formation is connected to Cu and not Si. This is also seen on Figure 4.3b, although the Cu on that particle might be in a Cu-Si alloy. There has been reported that coke formation takes place more rapidly on bulk Cu than on Si or Cu_3Si [3]. This claim can also be backed with the fact that depth profiles on Si particles shows almost no coke deposition, and coke is always present together with Cu. (Figure 4.3c, 4.3e and 4.3d).

The thickness of the coke deposition was different for all depth profiles. As only three depth particles were found to have a coke layer, the results are insufficient to see any trends.

Some of the elemental concentrations stay at very low values throughout the depth profile, but may not actually be present. Atomic percentages up to 10% may be produced from noise depending on the noise-to-signal ratio for the scans. This is because differentiated spectra with a noisy baseline stays noisy after differentiation, and AES quantification is based on peak-to-peak amplitude. Promoters Zn and Sn was not detected during any depth profiling. As the typical detection limit for AES is 0.1 at%, it suggests that Zn and Sn is not present at the surface [35]. Banholzer and Burrell reported that Sn is difficult to detect on the surface, as Sn, as well as Zn only concentrates on reacting Si areas [54].

4.2.1 Heterogeneity of Reacted Contact Mass - AES

AES depth profiles were difficult to reproduce due to the high heterogeneity of the reacted contact mass samples. This is evident by no depth profiles being reproduced with almost similar concentrations. The high variation within the samples has been reported during earlier research [55]. As the analysis area for the AES spectra is in the nm range, it makes the depth profiles quite specific to that spot. This means that inhomogeneity within the particle is not detected during depth profiling. Inhomogeneity between particles is also a factor that makes reproducing AES more difficult. An advantage of the small analysis spot is that it helps to see the local sample composition instead of an average composition one would acquire from a larger analysis area.

4.3 TPO Analysis

TPO analysis was performed for all unreacted contact mass and all reacted contact mass samples. Both TCD and MS signals were used to analyze the samples. Section 4.3.1 and 4.3.2 and presents and discusses results involving the TCD signal. Results gathered from the MS are discussed together with the technique in 4.3.3.

4.3.1 TCD Results

TCD signals for all contact mass samples (URCM, S13, S14, S17, S18, S19, and S20) are shown in Figure 4.4. Each spectrum is plotted with an arbitrary offset in the y-axis to better compare the results.

Normally, TPO coupled with TCD only measures oxygen consumption, since no products are formed when analyzing fresh classic catalysts. Oxygen consumption with O_2/He carrier gas produces positive TCD peaks. This is not the case here, as several products such as CO_2 , water, and other combustion products is formed from burning of coke. Formation of different products will change the thermal conductivity of the gas and affect the TCD signal.

The URCM sample shows two negative TCD peaks, with peak values at ~ 470 and $\sim 560^\circ C$. These peaks are not seen in any of the reacted contact mass samples. These peaks can be attributed to decomposition of $CuCl$. $CuCl$ melts at around $430^\circ C$ [56]. Zhou et al. reported that some $CuCl(l)$ evaporated at $488.5^\circ C$, while most aggregated into $Cu_3Cl_3(l)$ [57]. Aggregation of $CuCl$ into Cu_3Cl_3 , as shown in Equation 4.1, has been reported to happen over temperatures of $424^\circ C$ [58, 59].



The TCD peak at around $470^\circ C$ is based on this, most likely part of the $CuCl(l)$ evaporating. Cu_3Cl_3 evaporates at $667^\circ C$ and does not correlate with any TCD signal [57]. Marin et al. reported that $CuCl(g)$ is generated above $530^\circ C$ [60]. The second peak shoulder starts at $530^\circ C$, which makes this a possible assignation for the signal.

Si oxidizes in a wide temperature range from room temperature up to $1000^\circ C$ [61]. This makes it unlikely that the two TCD peaks for URCM are connected to Si oxidation.

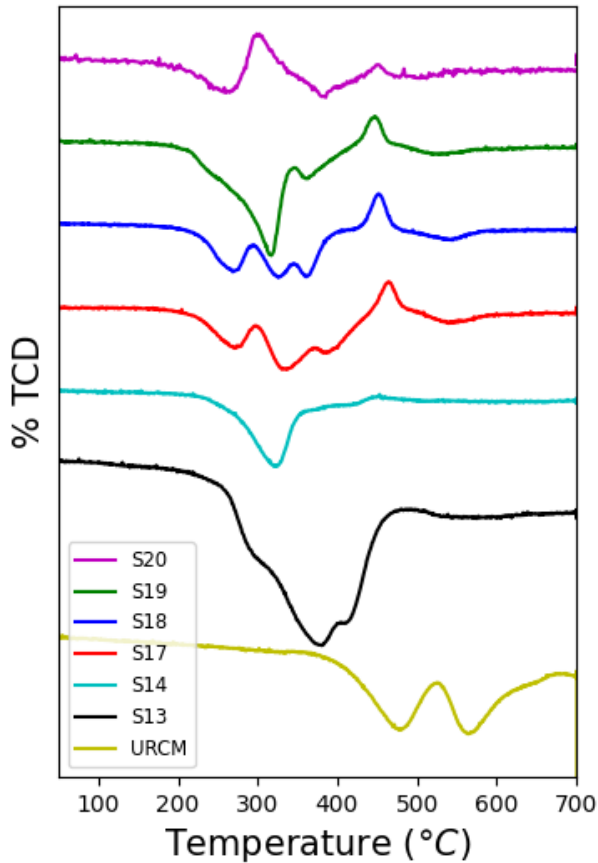


Figure 4.4: TCD signal versus temperature for all contact mass samples. The signals were offset along the y-axis for clarity.

4.3.2 TCD Results for Reacted Contact Mass

All reacted contact mass samples exhibit TCD signal changes only in the range of 200-500°C. The peaks detected for URCM are therefore not shared with the reacted samples. Contact mass samples reacted for 5 hours, S13(Zn and Sn promoted) and S14 (Sn promoted) exhibit wide negative peaks. The lowest TCD signal for S13 is at 380°C. The wide peak includes a visible shoulder at 320°C and a peak second peak at 410°C. A wide pos-

itive peak might be present at $\sim 480^\circ\text{C}$. The S14 negative signal peaks at 320°C , and also a small and wide positive peak at $\sim 450^\circ\text{C}$.

TCD results for contact mass reacted for 16 hours, S17(Zn and Sn promoted) and S18 (Sn promoted) are very similar. Both 16 hour samples exhibit negative peaks at 270°C and 325°C . A third negative peak is seen for both samples but with some shift between the samples. The peak of the third signal is 385°C and 360°C for S17 and S18, respectively. S17 and S18 show a well-defined positive peak with respective maximum values at 465°C and 450° .

Samples reacted for 40 hours, S19(Zn and Sn promoted) and S20(Sn promoted) show some divergence. The S19 TCD signal shows some of the same peaks as S17 and S18. Two negative peaks at 315°C and 360°C , and the positive peak at 450°C is seen for all three samples. A small shoulder can also be seen at the start of the negative peaks that might be attributed to a peak at around 270° seen for S17 and S18. TCD signal from S20 shows more noise than the other samples. It exhibits the negative peaks seen for some other samples at 260°C and 380°C , as well as the positive peak at 450°C . The S20 signal also has a positive peak at 300°C .

As mentioned before, solely oxygen consumption should yield positive peaks for this TPO setup with O_2/He carrier gas. However, CO_2 production will take place due to combustion of coke formation, and the product of the gas stream can produce negative TCD signals. CO_2 (and CO) has a lower thermal conductivity compared to He (Table 3.4, Section 3.4), corresponding to negative peaks.

The negative peak at $260\text{-}270^\circ\text{C}$ region can therefore be attributed to CO_2 production and combustion of coke. Wessel and Rethwisch reported two coke formation peaks at $\sim 257^\circ\text{C}$ and $\sim 342^\circ\text{C}$ [3]. The first peak, designated as α -coke fits with the TCD signal. β -coke, designated to $\sim 342^\circ\text{C}$ falls in between the two other TCD peaks[3]. The TCD peak at $315\text{-}325^\circ$ depending on the sample is the largest peak and is most likely coke. The temperature values are close enough to correlate this peak to β -coke.

Coke classification for TPO analysis is based on oxidation temperature. Lower oxidation temperatures, typically $\leq 400^\circ\text{C}$ can be attributed to soft coke. Soft coke often consists of primarily amorphous structures, alkylated aromatics, and small amounts of polyaromatics. Hard coke, on the other hand, has a more graphitic structure and consists of predominantly polycondensed aromatic compounds [62]. Muhammad et al. reported that hard coke was not removed from the sample before 600°C [63]. Coke formed on

the reacted contact mass samples was classified as soft coke. Variation of peak temperature between samples was seen and would mean varying coke reactivity.

Previous TGA studies on reacted contact mass samples reported coke formation based on CO_2 signal from MS results. This coke was oxidized with a peak temperature between $290^\circ C$ and $336^\circ C$ and was reported as soft coke [55].

The positive peak seen for all samples at $\sim 450^\circ C$ might be due to O_2 consumption. As coke deposition layers are burned off the contact mass, easily oxidized active sites become exposed [3]. Oxidation of these surfaces would lead to positive TCD peaks. The peak comes directly after the burning of coke, making oxidation a plausible cause. The positive peak is barely visible for samples reacted for 5 hours (S13 and S14). These samples should have less coke, and should therefore get less reduced surface metal exposed after coke combustion. Previous XRD study of the contact mass samples has shown substantial amounts of elemental Cu on samples reacted for 16 and 40 hours [55].

One of the goals for TPO analysis was to quantify coke formation. Thermal conductivities for He mixtures are nonlinear in relation to concentration, which makes quantification of TCD results from TPO practically impossible [64].

The S13 reacted contact mass sample is somewhat of an anomaly compared to the other reacted contact mass samples. The whole negative TCD area is larger than for all other contact mass samples, and all visible peaks are shifted to higher temperatures. Results were not reproduced due to instrument problems and time restraints. As samples S14-S19 show a greater likeness in peak positions and peak area, it is assumed that the S13 TCD signal is an anomaly.

The positive peak for the S20 sample between the negative peaks is not treated as a product of the sample composition since it is not seen for any other sample. It is therefore not further discussed. The S20 signal is also quite different compared to the other contact mass samples. It was attempted to reproduce this signal which is shown in Figure B.2 (Appendix B). The S20 sample is here labeled as S20-01, and S20-02 is the new run. These TPO results are plotted with time on the x-axis and TCD and temperature($^\circ C$) on the primary and secondary y-axis, respectively. This is due to S20-02 showing TCD signal during the temperature hold on $700^\circ C$. The two TPO signals for S20 are vastly different. Due to the S20-02 sig-

nal differing from all the other TCD signals, S20-01 is chosen as the most representative one. The different result from S20-02 is treated as a problem due to the TPO technique and/or instrument.

The surface oxidation peak after coke burning shows the only indication of any trend. This shows a marginally smaller peak for samples reacted for 5 hours (S13 and S14), compared to 16h (S17 and S18) and 40h (S19 and S20). There is however no size difference in this positive peak between samples S17, S18, and S19. S20 exhibits a smaller peak at this temperature, but this is disregarded as less carbon formation due to the strangeness of the rest of the signal. This might not mean that S19 has the same amount of coke deposition, but that the same amount of surface was exposed for oxidation. No obvious trends can be seen for the coke peaks related to reaction time and Zn promotion.

4.3.3 MS Results from TPO Analysis

All of the TPO experiments conducted were coupled with an MS detector. The main focus for the MS was detection of CO_2 ($m/z=44$) and H_2O ($m/z=18$). C/H ratio is an important measurement for analysis for coke formation. For TPO coupled with MS, analysis of hydrogen content is usually measured from the H_2O signal and carbon content from CO_2 signal. It was not possible to detect hydrogen content with the used instrument as any produced H_2O is removed from the flue gas with a trap containing desiccant. Figure 4.5 shows MS spectra for all reacted contact mass samples except S20. MS CO_2 signal and temperature ($^{\circ}C$) is plotted on the primary and secondary y-axis, respectively. Both are plotted against time (min) on the x-axis. Time is chosen for the x-axis instead of temperature since the MS peaks continue after heating up to $700^{\circ}C$.

There were several issues with interpreting the MS results. The MS CO_2 signal does not increase before $\sim 350^{\circ}C$. The signal peaks at varying temperatures between 530 and $700^{\circ}C$, with S17 peaking after the temperature ramp. After peak temperatures are reached, all peaks decrease slowly and never reach the MS baseline within the analyzed time frame. This makes it hard to accurately quantify the coke deposition. The signal delay compared to TCD results can be attributed to the instrument setup. The line from the TPO reactor and TCD to the MS instrument is quite long and has been known to cause a signal delay. It has also been detected varying delay for individual TPR/TPO experiments with the instrument. There is

therefore not a measured delay one can take into account to correct MS spectra.

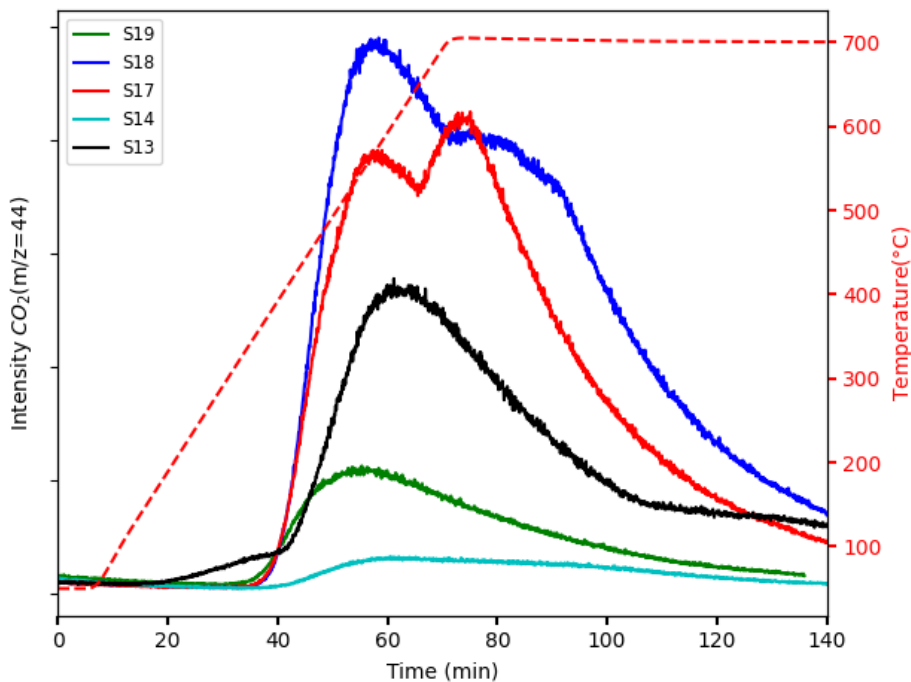


Figure 4.5: CO_2 MS signal ($m/z=44$) and temperature versus time during TPO experiment for all reacted contact mass samples except S20.

The MS intensity for the reacted contact mass samples varies greatly with no apparent trend. The MS CO_2 signal for all reacted contact mass samples is showed in Figure B.3 (Appendix B). The S20 MS intensity is over one order of magnitude greater than any of the other contact mass samples. The intensity difference is also seen between the rest of the samples in Figure 4.5. There seems to be no logical trend to the peak intensity of the MS signal. S17 and S18 show two distinct peaks that may correspond to two coke peaks seen in TCD results. Due to delay issues and generally inconclusive results from MS spectra, the results are not further discussed. For further MS coupled TPO with the used instrument it is recommended to modify the instrument to improve the results or use a more suited instrument.

4.4 FT-IR Investigation of Reacted Contact Mass

Figure 4.6 shows FT-IR spectra for all reacted contact mass samples in the range of $4000\text{-}600\text{ cm}^{-1}$. Each spectrum has been baseline corrected in the FT-IR software (OPUS). Multiple peaks and signals can be found in the range between 1800 and 2800 cm^{-1} . All of the signals in this range are attributed to the anvil and/or crystal of the FT-IR instrument, as the signals are reproduced for all samples analyzed with the instrument. The range between 1800 and 2800 cm^{-1} does not exhibit any signal from the sample as the signal is entirely reproduced with completely different samples.

An overview of all FT-IR peaks detected from the sample and their assignment is shown in Table 4.1.

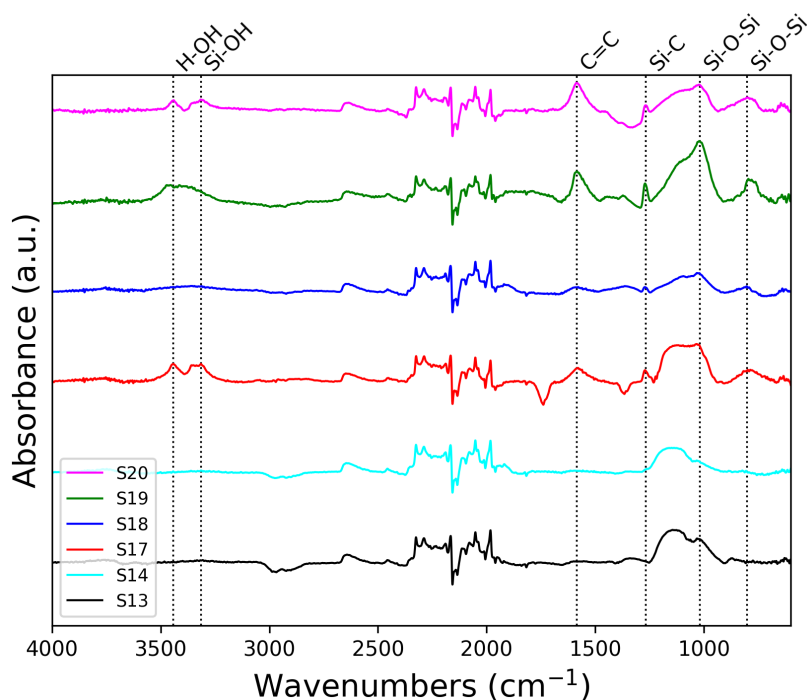


Figure 4.6: FT-IR results of all reacted contact mass samples in the full wavenumber region of $600\text{-}4000\text{ cm}^{-1}$. The equipment was purged with N_2 gas for to minimize the effect of atmospheric moisture and CO_2 and increase the intensity of IR radiations. All spectra have been baseline corrected.

Table 4.1: Summary of FT-IR peaks detected for the reacted contact mass samples. The approximate peak value (wavenumber), the designated bond and sources backing the designation is shown.

Wavenumber (cm ⁻¹)	Group	Source
3442	H-OH/Si-OH	[65, 66, 67]
3315	Si-OH	[65, 66, 67]
1584	C=C	[67, 68, 69]
1267	Si-C	[66, 25, 70, 71]
1018	Si-O-Si	[25, 65, 66, 70, 71, 72, 73, 74, 75]
800	Si-O/Si-O-Si	[72, 76]

In the high wavenumber range, there are only two visible peaks for the reacted contact mass samples as seen in Figure 4.7. One peak at 3442 cm⁻¹ and one at 3315 cm⁻¹. The region between 3500-3200 cm⁻¹ is assigned to O-H stretching [67, 66]. The peak at 3315 cm⁻¹ can specifically be assigned to Si-OH [65], while the peak at 3442 cm⁻¹ can be assigned to either H-OH or Si-OH. The two peaks are either both present or not visible, as seen in Figure 4.6. These peaks can be somewhat assigned to oxidation of Si, as they are more present in samples exposed to air longer (Figure A.1, Appendix A).

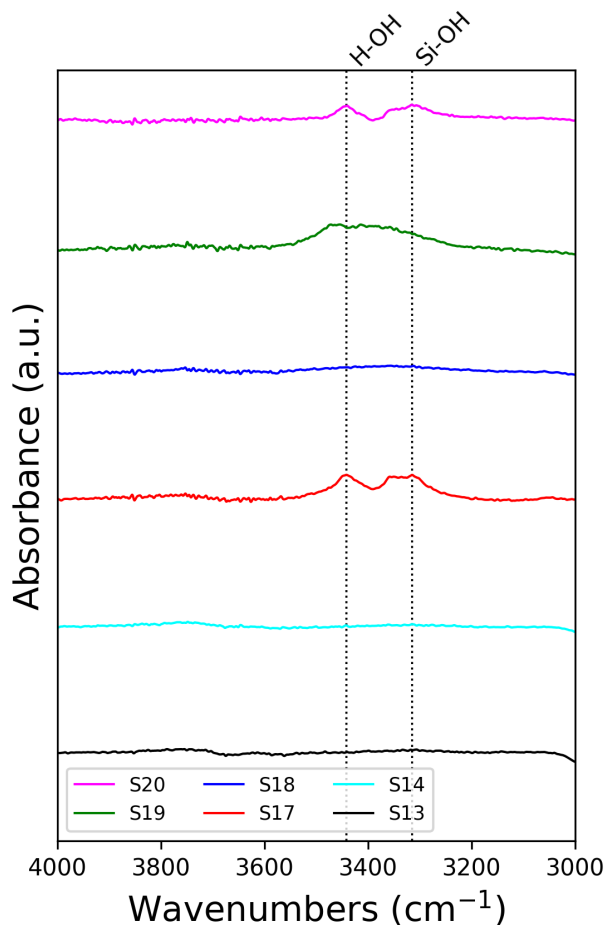


Figure 4.7: FT-IR results of all reacted contact mass samples in the high wavenumber region, $3000\text{-}4000\text{ cm}^{-1}$. The equipment was purged with N_2 gas to minimize the effect of atmospheric moisture and CO_2 and increase the intensity of IR radiations. All spectra have been baseline corrected.

Figure 4.8 shows a more detailed view of FT-IR results in the $1700\text{-}600\text{ cm}^{-1}$ region. The peak at 1584 cm^{-1} can be assigned to a C=C stretching bond [65, 67, 68, 69]. The thin peak at 1267 cm^{-1} is assigned to the Si-C bond [72]. The presence of a peak at 1018 cm^{-1} can be attributed to silicon-oxygen vibrations, specifically Si-O-Si [25, 70]. The wide peak between $1200\text{-}1000\text{ cm}^{-1}$ may contain contributions from several other

silicon-oxygen vibrations which have spectral values in this region [25, 70].

The last easily recognisable peak is at around 800 cm^{-1} . This peak can be attributed to several relevant groups:

- Si-CH₃ [72]
- Si-O-Si [66, 73, 74, 77]
- Si-O [76]
- Si-C (silicon carbide) [65]

The most likely assignation for this peak is an oxide layer, either Si-O-Si or Si-O bond. This is due to the presence of this peak somewhat correlates with the presence of oxidation peaks at high wavenumbers as seen in Figure 4.7.

The peak at 1584 cm^{-1} has been attributed to highly unsaturated carbonaceous deposits, also called hard coke [78, 79, 80]. The peak has been reported to be reliable for measuring the amount of coke deposition on reacted catalysts [78, 81]. The presence of unsaturated coke increases with reaction time as seen in Figure 4.8. The peak is not visible on contact mass spectra reacted for 5 hours (S13 and S14), visible after 16 hours (S17 and S18), and shows an increased intensity after 40 hour (S19 and S20). Hence, a longer reaction time shows an increasing amount of coke.

The Si-C bond (1267 cm^{-1}) shows the presence of CH_3 adsorbed on the Si surface [70, 82]. This bond is however not connected to coke formation in any previous literature. For the reacted contact mass samples, its presence seems to correlate to the C=C peak.

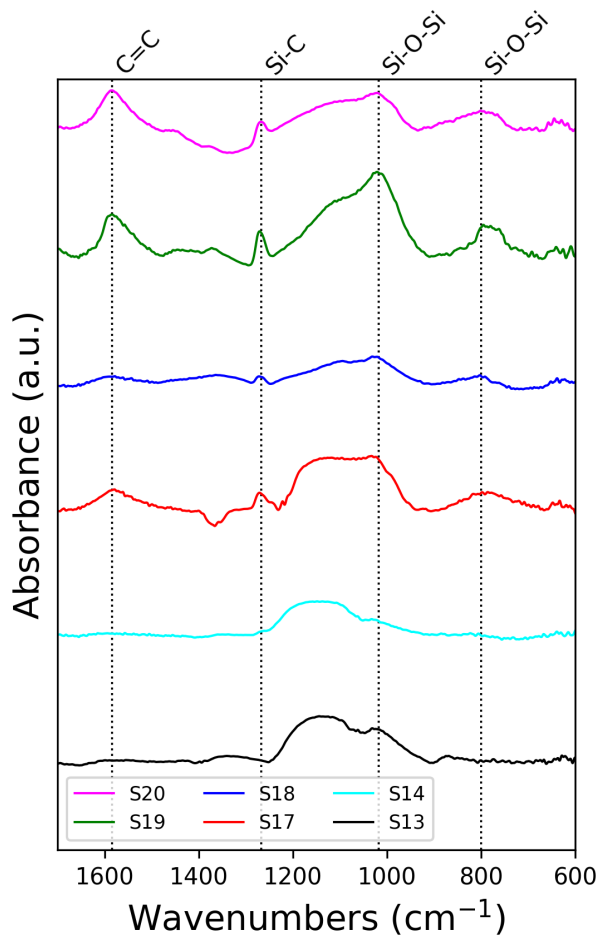


Figure 4.8: FT-IR results of all reacted contact mass samples in the high wavenumber region, 600-1700 cm^{-1} . The equipment was purged with N_2 gas to minimize the effect of atmospheric moisture and CO_2 and increase the intensity of IR radiations. All spectra have been baseline corrected.

Conclusion

This Master's thesis was carried out in order to investigate and characterize coke formation during the direct synthesis of dimethyldichlorosilane. Deactivation by coke deposition has a great impact on the industrial operation of the direct synthesis, but has not received much attention in research. The coke composition and reactivity were investigated to further develop an understanding of the coke formation mechanism. The unreacted contact mass sample and a series of reacted contact mass samples with varying reaction times and Zn promotion were characterized by Auger electron spectroscopy (AES), depth profiling, temperature-programmed oxidation (TPO) and Fourier transform infrared spectroscopy (FT-IR).

The characteristic AES carbon peak (C(KLL)) showed that reacted contact mass samples contain coke formation with amorphous and graphitic structure. There was no apparent difference in coke morphology with and without Zn promotion. Samples reacted for 40 hours showed peak characteristics closer to graphite than samples reacted for a shorter period. This suggests that the coke morphology becomes more graphitic with increasing reaction time.

Depth profiling revealed that contact mass samples consist of mostly homogeneous Cu or Si beneath the surface layer. Particles containing mostly Cu were most likely to have a coke deposition layer, while Si particles for the most part contained no coke. AES depth profiling on reacted contact mass detected high heterogeneity in the contact mass samples. Different particles and different spots on the same particle showed a high divergence in composition. This makes it hard to reproduce AES results.

TCD results from TPO revealed combustion of coke for all contact mass samples at $\sim 270^{\circ}\text{C}$ and $\sim 380^{\circ}\text{C}$, with some differences. No apparent trend could be attributed to these peaks. Another TCD peak at a higher temperature was attributed to oxidation of exposed surface after coke removal. This peak revealed that samples reacted for 16 hours and 40 hours had significantly more of the surface exposed than samples reacted for 5 hours.

FT-IR investigations revealed signals attributed to highly unsaturated coke. This peak was not visible after 5 hours of reaction time, but visible at 16 and 40 hours at somewhat comparable intensities.

Chapter 6

Future Work

Several aspects of the direct synthesis of dimethyldichlorosilane need further investigation. The techniques used in this thesis work are new to this project and can be improved further.

Surface analysis of reacted contact mass samples should be continued. AES surface analysis and depth profiling results should be reproduced on a larger scale due to the heterogeneity of the samples. AES chemical analysis of other elements than carbon can be beneficial to see in which oxidation state they are present. Performing AES depth profiles with settings for higher energy resolution (M2/M3) would get more information on the chemical state of the present elements. This could also get improved results of the coke structure.

SEM was used as a support method for AES sample positioning. SEM or S(T)EM investigation can find visual differences between Si and Cu particles e.g. size distribution. SEM or S(T)EM coupled with energy-dispersive X-ray spectroscopy(EDX) should be used to study the buildup of coke on the surface.

TPO analysis can be improved by either modifying the current setup or using another instrument. TPO coupled with MS is preferred as one can see the H/C-ratio of the coke. This is not possible with the current TPO setup and should be changed.

References

- [1] W.J. Ward et al. “Catalysis of the Rochow Direct Process”. In: *Journal of Catalysis* 100.1 (1986), pp. 240–249. ISSN: 0021-9517. DOI: [https://doi.org/10.1016/0021-9517\(86\)90089-8](https://doi.org/10.1016/0021-9517(86)90089-8).
- [2] Dietmar Seyferth. “Dimethyldichlorosilane and the Direct Synthesis of Methylchlorosilanes. The Key to the Silicones Industry”. In: *Organometallics* 20.24 (2001), pp. 4978–4992. DOI: [10.1021/om0109051](https://doi.org/10.1021/om0109051).
- [3] T.J. Wessel and D.G. Rethwisch. “Deactivation of CuSi and CuZn-SnSi Due to Coke Formation during the Direct Synthesis of Methylchlorosilanes”. In: *Journal of Catalysis* 161.2 (1996), pp. 861–866. ISSN: 0021-9517. DOI: <https://doi.org/10.1006/jcat.1996.0248>.
- [4] Yu Zhang et al. “Recent Advances in Rochow-Müller Process Research: Driving to Molecular Catalysis and to A More Sustainable Silicone Industry”. In: *ChemCatChem* 11.12 (2019), pp. 2757–2779. DOI: <https://doi.org/10.1002/cctc.201900385>.
- [5] Gerhard Ertl et al. *Handbook of heterogeneous catalysis*. Vol. 2. Citeseer, 1997.
- [6] André Colas. “Silicones: preparation, properties and performance”. In: Citeseer, 2005.
- [7] Jörg Acker and Klaus Bohmhammel. “Thermodynamic assessment of the copper catalyzed direct synthesis of methylchlorosilanes”. In: *Journal of Organometallic Chemistry* 693.15 (2008), pp. 2483–2493.

-
- [8] Michael P. Clarke. "The direct synthesis of methylchlorosilanes". In: *Journal of Organometallic Chemistry* 376.2 (1989), pp. 165 – 222. DOI: [https://doi.org/10.1016/0022-328X\(89\)85131-9](https://doi.org/10.1016/0022-328X(89)85131-9).
- [9] Wuxi Luo et al. "Surface morphology and catalytic activity of the contact mass in organosilane synthesis". In: *Chemical Engineering Communications* 193.6 (2006), pp. 754–763. DOI: 10.1080/00986440500267162.
- [10] I. Chorkendorff. *Concepts of modern catalysis and kinetics*. 2nd, rev. and enl. ed. Weinheim: Wiley-VCH, 2007. ISBN: 9783527316724.
- [11] JP Agarwala and John L Falconer. "Kinetics of methylchlorosilane formation on Zn-promoted Cu₃Si". In: *International journal of chemical kinetics* 19.6 (1987), pp. 519–537.
- [12] WANG Chao et al. "A bi-component Cu catalyst for the direct synthesis of methylchlorosilane from silicon and methyl chloride". In: *Chinese Journal of Chemical Engineering* 22.3 (2014), pp. 299–304.
- [13] Timothy C Frank and John L Falconer. "Silane formation on silicon: reaction kinetics and surface analysis". In: *Langmuir* 1.1 (1985), pp. 104–110.
- [14] Wuxi Luo et al. "Effect of CuCl Particle Size on the Reduction Reaction by Silicon in Preparation of Contact Mass Used for Methylchlorosilane Synthesis". In: *Industrial & Engineering Chemistry Research* 45.1 (2006), pp. 129–133. DOI: 10.1021/ie058044+.
- [15] Xin Chen et al. "Solvothermal synthesis of copper (I) chloride microcrystals with different morphologies as copper-based catalysts for dimethyldichlorosilane synthesis". In: *Journal of colloid and interface science* 404 (2013), pp. 16–23.
- [16] J. Acker et al. "The reactivity in the system CuCl-Si related to the activation of silicon in the Direct Synthesis". In: *Silicon Chemistry* 2.3 (2003), pp. 195–206.

-
- [17] R.J.H. Voorhoeve and J.C. Vlugter. “Mechanism and kinetics of the metal-catalyzed synthesis of methylchlorosilanes: III. The catalytically active form of the copper catalyst”. In: *Journal of Catalysis* 4.2 (1965), pp. 123–133. ISSN: 0021-9517. DOI: [https://doi.org/10.1016/0021-9517\(65\)90003-5](https://doi.org/10.1016/0021-9517(65)90003-5).
- [18] R.J.H. Voorhoeve et al. “Mechanism and kinetics of the metal-catalyzed synthesis of methylchlorosilanes: I. The synthesis of methylchlorosilanes in a fluid bed”. In: *Journal of Catalysis* 3.5 (1964), pp. 414–425. ISSN: 0021-9517. DOI: [https://doi.org/10.1016/0021-9517\(64\)90144-7](https://doi.org/10.1016/0021-9517(64)90144-7).
- [19] Timothy C. Frank et al. “Catalytic formation of silanes on copper-silicon alloys”. In: *Journal of Catalysis* 91.1 (1985), pp. 44–53. ISSN: 0021-9517. DOI: [https://doi.org/10.1016/0021-9517\(85\)90286-6](https://doi.org/10.1016/0021-9517(85)90286-6).
- [20] G. Weber et al. “Effect of small amounts of various additives on the reaction between a single crystal of silicon and fused copper chloride”. In: *Reactivity of Solids* 6.1 (1988), pp. 75–93. ISSN: 0168-7336. DOI: [https://doi.org/10.1016/0168-7336\(88\)80047-0](https://doi.org/10.1016/0168-7336(88)80047-0).
- [21] Chao Wang et al. “Promoter Effects of Zn and Sn in the Direct Synthesis of Methylchlorosilanes”. In: *Industrial & Engineering Chemistry Research* 52.15 (2013), pp. 5282–5286. DOI: [10.1021/ie303515q](https://doi.org/10.1021/ie303515q).
- [22] J.M. Bablin et al. “Effect of low aluminum silicon on the direct process”. In: *Industrial & engineering chemistry research* 42.15 (2003), pp. 3555–3565.
- [23] L.D. Gasper-Galvin et al. “Role of metallic promoters in the direct synthesis of methylchlorosilanes”. In: *Journal of Catalysis* 128.2 (1991), pp. 468–478. ISSN: 0021-9517. DOI: [https://doi.org/10.1016/0021-9517\(91\)90304-M](https://doi.org/10.1016/0021-9517(91)90304-M).
- [24] S.J. Potochnik and J.L. Falconer. “The Effect of Zn Promoter on Enhanced Diffusion During Catalytic Formation of Methylchlorosilanes”. In: *Journal of Catalysis* 147.1 (1994), pp. 101–106. ISSN: 0021-9517. DOI: <https://doi.org/10.1006/jcat.1994.1119>.
-

-
- [25] Alexander D. Gordon et al. "Effects of multiple promotion of the direct synthesis contact mass with P, Zn, and Sn on the synthesis of methylchlorosilanes". In: *Catalysis letters* 133.1-2 (2009), p. 14. DOI: <https://doi.org/10.1007/s10562-009-0172->.
- [26] Zhang Lei et al. "Effects of double promoters on direct synthesis of triethoxysilane in gas–solid stirred fluidized bed". In: *Applied Organometallic Chemistry* 25.7 (2011), pp. 508–513. DOI: <https://doi.org/10.1002/aoc.1794>.
- [27] Pio Forzatti and Luca Lietti. "Catalyst deactivation". In: *Catalysis today* 52.2-3 (1999), pp. 165–181.
- [28] Calvin H. Bartholomew. "Mechanisms of catalyst deactivation". In: *Applied Catalysis A: General* 212.1 (2001), pp. 17 –60. ISSN: 0926-860X. DOI: [https://doi.org/10.1016/S0926-860X\(00\)00843-7](https://doi.org/10.1016/S0926-860X(00)00843-7).
- [29] P.G. Menon. "Coke on catalysts-harmful, harmless, invisible and beneficial types". In: *Journal of Molecular Catalysis* 59.2 (1990), pp. 207–220.
- [30] M. Guisnet and P. Magnoux. "Organic chemistry of coke formation". In: *Applied Catalysis A: General* 212.1-2 (2001), pp. 83–96.
- [31] V. Bažant. "Direct Synthesis of organohalogenosilanes". In: *Pure and Applied Chemistry* 13.1-2 (1Jan. 1966), pp. 313 –328. DOI: <https://doi.org/10.1351/pac196613010313>.
- [32] Johannes W. Niemantsverdriet. *Spectroscopy in catalysis*. Wiley Online Library, 2007.
- [33] Joseph I. Goldstein et al. *Scanning electron microscopy and X-ray microanalysis*. Springer, 2017.
- [34] Nicolas Pauly et al. "LMM Auger primary excitation spectra of copper". In: *Surface science* 630 (2014), pp. 294–299.
- [35] Siegfried Hofmann. *Auger-and X-ray photoelectron spectroscopy in materials science: a user-oriented guide*. Vol. 49. Springer Science & Business Media, 2012.
- [36] G.E. McGuire. *Auger electron spectroscopy reference manual*. Springer, 1980.

-
- [37] Benjamin Carroll. “Auger electron spectroscopy reference manual”. In: *Microchemical journal*. 26.3 (1981), p. 444.
- [38] Lawrence E Davis. *Handbook of Auger Electron Spectroscopy: A Reference Book of Standard Data for Identification and Interpretation of Auger Electron Spectroscopy Data*. Physical Electronics Industries, 1976.
- [39] Yongfa Zhu and Lili Cao. “Auger chemical shift analysis and its applications to the identification of interface species in thin films”. In: *Applied surface science* 133.3 (1998), pp. 213–220.
- [40] TW Haas et al. “Chemical effects in Auger electron spectroscopy”. In: *Journal of Applied Physics* 43.4 (1972), pp. 1853–1860.
- [41] CD Wagner. “Chemical shifts of Auger lines, and the Auger parameter”. In: *Faraday Discussions of the Chemical Society* 60 (1975), pp. 291–300.
- [42] S Hofmann. “Sputter depth profile analysis of interfaces”. In: *Reports on Progress in Physics* 61.7 (1998), p. 827.
- [43] Graham C Smith. “Structure Determination of Inhomogenous Samples”. In: *Surface Analysis by Electron Spectroscopy*. Springer, 1994, pp. 75–92.
- [44] Antonella Gervasini. “Temperature Programmed Reduction/Oxidation (TPR/TPO) Methods”. In: *Calorimetry and Thermal Methods in Catalysis*. Springer, 2013, pp. 175–195.
- [45] C.F. Poole. “GAS CHROMATOGRAPHY — Detectors”. In: *Encyclopedia of Analytical Science (Second Edition)*. Ed. by Paul Worsfold et al. Second Edition. Oxford: Elsevier, 2005, pp. 95–105. DOI: <https://doi.org/10.1016/B0-12-369397-7/00222-3>.
- [46] CA Querini and SC Fung. “Coke characterization by temperature programmed techniques”. In: *Catalysis today* 37.3 (1997), pp. 277–283.
- [47] Emily Moore. “Fourier transform infrared spectroscopy (FTIR): Methods, analysis and research insights”. In: *Fourier Transform Infrared Spectroscopy (FTIR): Methods, Analysis and Research Insights*. 2016, pp. 1–129.
-

-
- [48] Takeshi Hasegawa. *Quantitative infrared spectroscopy for understanding of a condensed matter*. Springer, 2017.
- [49] Brian C Smith. *Fundamentals of Fourier transform infrared spectroscopy*. CRC press, 2011.
- [50] Anand Subramanian and Luis Rodriguez-Saona. “Chapter 7 - Fourier Transform Infrared (FTIR) Spectroscopy”. In: *Infrared Spectroscopy for Food Quality Analysis and Control*. Ed. by Da-Wen Sun. San Diego: Academic Press, 2009, pp. 145–178. DOI: <https://doi.org/10.1016/B978-0-12-374136-3.00007-9>.
- [51] JEOL Ltd. *Auger Microprobe*. URL: <https://www.jeol.co.jp/en/science/am.html>. (Accessed: 14.05.2021).
- [52] Marcia L Huber and Allan H Harvey. “Thermal conductivity of gases”. In: *CRC Handbook of Chemistry and Physics* (2011), pp. 6–2240.
- [53] PG Lurie and JM Wilson. “The diamond surface: II. Secondary electron emission”. In: *Surface Science* 65.2 (1977), pp. 476–498.
- [54] William F Banholzer and Michael C Burrell. “Characterization of reactive areas in the direct process for the production of methylchlorosilanes”. In: *Journal of Catalysis* 114.2 (1988), pp. 259–270.
- [55] Hammad Farooq. “Effect of CuCl and Zn on Cu₃Si Formation and Coke Deposition in the Direct Synthesis of Dimethyldichlorosilane In collaboration with Elkem”. MA thesis. NTNU, Aug. 2020.
- [56] Z Wang et al. “Thermodynamics and kinetics of the thermal decomposition of cupric chloride in its hydrolysis reaction”. In: *Journal of Thermal Analysis and Calorimetry* 119.2 (2015), pp. 815–823.
- [57] Shuiliang Zhou et al. “Evaporation and decomposition of eutectics of cupric chloride and sodium chloride”. In: *Journal of Thermal Analysis and Calorimetry* 129.3 (2017), pp. 1445–1452.
- [58] Harald Schäfer. “Gaseous Chloride Complexes with Halogen Bridges—Homo-Complexes and Hetero-Complexes”. In: *Angewandte Chemie International Edition in English* 15.12 (1976), pp. 713–727.

-
- [59] David L Hilden and NW Gregory. “Vapor-phase absorbance and thermodynamic properties of cuprous chloride and cuprous bromide”. In: *The Journal of Physical Chemistry* 76.11 (1972), pp. 1632–1637.
- [60] GD Marin et al. “X-ray diffraction study of multiphase reverse reaction with molten CuCl and oxygen”. In: *Thermochimica acta* 524.1-2 (2011), pp. 109–116.
- [61] Hisham Z Massoud. “The onset of the thermal oxidation of silicon from room temperature to 1000° C”. In: *Microelectronic Engineering* 28.1-4 (1995), pp. 109–116.
- [62] Moritz Wolf et al. “Coke formation during propane dehydrogenation over Ga- Rh supported catalytically active liquid metal solutions”. In: *ChemCatChem* 12.4 (2020), p. 1085.
- [63] Ishaka Muhammad et al. “Catalytic degradation of linear low-density polyethylene over HY-zeolite via pre-degradation method”. In: *Journal of Analytical and Applied Pyrolysis* 138 (2019), pp. 10–21.
- [64] C.J. Cowper. “GAS ANALYSIS: GAS CHROMATOGRAPHY”. In: *Encyclopedia of Separation Science*. Ed. by Ian D. Wilson. Oxford: Academic Press, 2000, pp. 2925–2932. ISBN: 978-0-12-226770-3. DOI: <https://doi.org/10.1016/B0-12-226770-2/00491-9>.
- [65] Philip J Launer. “Infrared analysis of organosilicon compounds: spectra-structure correlations”. In: *Silicone compounds register and review* 100 (1987).
- [66] F Rubio et al. “A FT-IR study of the hydrolysis of tetraethylorthosilicate (TEOS).” In: *Spectroscopy Letters* 31.1 (1998), pp. 199–219.
- [67] Merck KGaA. *IR Spectrum Table & Chart*. URL: https://www.sigmaaldrich.com/technical-documents/articles/biology/ir-spectrum-table.html?fbclid=IwAR2Fh-u4CtTcVop_GN8pmH2BK_3A7-tnKPFBlacVFtCos2v7UzFXBsPDJv0#ir-table-by-compound. (Accessed: 28.05.2021).
-

-
- [68] Heung Kim and Marek W Urban. “Reaction sites on poly (dimethylsiloxane) elastomer surfaces in microwave plasma reactions with gaseous imidazole: a spectroscopic study”. In: *Langmuir* 12.4 (1996), pp. 1047–1050.
- [69] V Arjunan et al. “FTIR and FTR spectral studies of 2-amino-6-bromo-3-formylchromone”. In: *Spectrochimica Acta Part A: Molecular and Biomolecular Spectroscopy* 60.5 (2004), pp. 995–1000.
- [70] Alexander D. Gordon et al. “Effects of individual promoters on the Direct Synthesis of methylchlorosilanes”. In: *Journal of Catalysis* 266.2 (2009), pp. 291–298. ISSN: 0021-9517. DOI: <https://doi.org/10.1016/j.jcat.2009.06.026>.
- [71] Yajun Huang et al. “Organic solvent-saving preparation of water glass based aerogel granules under ambient pressure drying”. In: *Journal of Non-Crystalline Solids* 521 (2019), p. 119507.
- [72] Jerzy J. Chruściel et al. “Synthesis, characterization and microstructure of new liquid poly (methylhydrosiloxanes) containing branching units SiO₄/2”. In: *Polymers* 10.5 (2018), p. 484.
- [73] Xiaoxu Wu et al. “Effects of various methylchlorosilanes on physicochemical properties of ambient pressure dried silica aerogels”. In: *Journal of Nanoparticle Research* 21.11 (2019), pp. 1–13.
- [74] Min Tae Kim. “Deposition behavior of hexamethydisiloxane films based on the FTIR analysis of Si–O–Si and Si–CH₃ bonds”. In: *Thin Solid Films* 311.1-2 (1997), pp. 157–163.
- [75] Hongmei Jiang et al. “Kinetic study of methyltriethoxysilane (MTES) hydrolysis by FTIR spectroscopy under different temperatures and solvents”. In: *Vibrational spectroscopy* 46.1 (2008), pp. 1–7.
- [76] Shang-Chieh Hou et al. “Mechanochemical synthesis of Si/Cu 3 Si-based composite as negative electrode materials for lithium ion battery”. In: *Scientific reports* 8.1 (2018), pp. 1–11.
- [77] Zaidong Shao et al. “Superhydrophobic sodium silicate based silica aerogel prepared by ambient pressure drying”. In: *Materials Chemistry and Physics* 141.1 (2013), pp. 570–575.
- [78] Chiuping Li et al. “In-situ FTIR investigation of coke formation on USY zeolite”. In: *Applied surface science* 81.4 (1994), pp. 465–468.

-
- [79] Donna G. Blackmond et al. "In situ Fourier transform infrared spectroscopy study of HY cracking catalysts: Coke formation and the nature of the active sites". In: *Journal of Catalysis* 78.1 (1982), pp. 34–43.
- [80] Hellmut G. Karge and Edwin P Boldingh. "In-situ IR investigation of coke formation on dealuminated mordenite catalysts". In: *Catalysis Today* 3.1 (1988), pp. 53–63.
- [81] D. Eisenbach and E. Gallei. "Infrared spectroscopic investigations relating to coke formation on zeolites: I. Adsorption of hexene-1 and n-hexane on zeolites of type Y". In: *Journal of Catalysis* 56.3 (1979), pp. 377–389.
- [82] John A. Glass Jr. et al. "Reaction of methanol with porous silicon". In: *Surface science* 338.1-3 (1995), pp. 125–137.

Appendix

A Additional FT-IR Figures

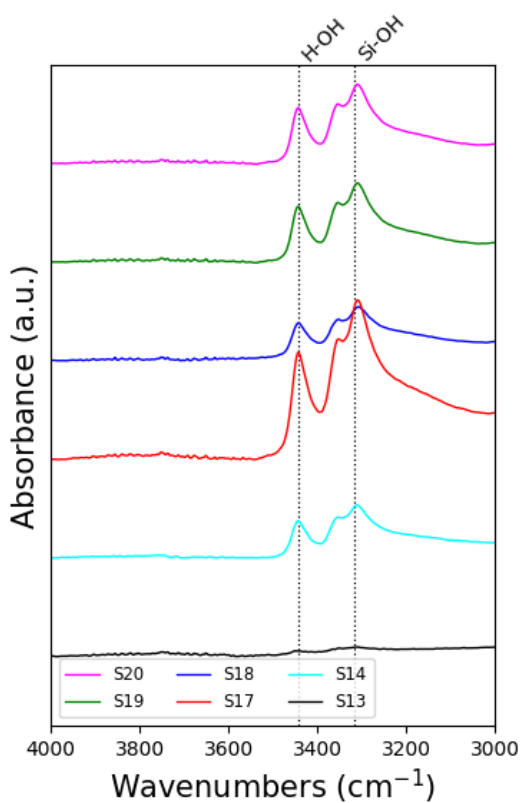


Figure A.1: FT-IR results of all reacted contact mass samples in the high wavenumber region, 3000-4000 cm^{-1} . The reacted contact mass samples have been exposed to air, and not purged with N_2 . All spectra have been baseline corrected. These FT-IR spectra were collected without N_2 purging.

B Additional TPO Figures

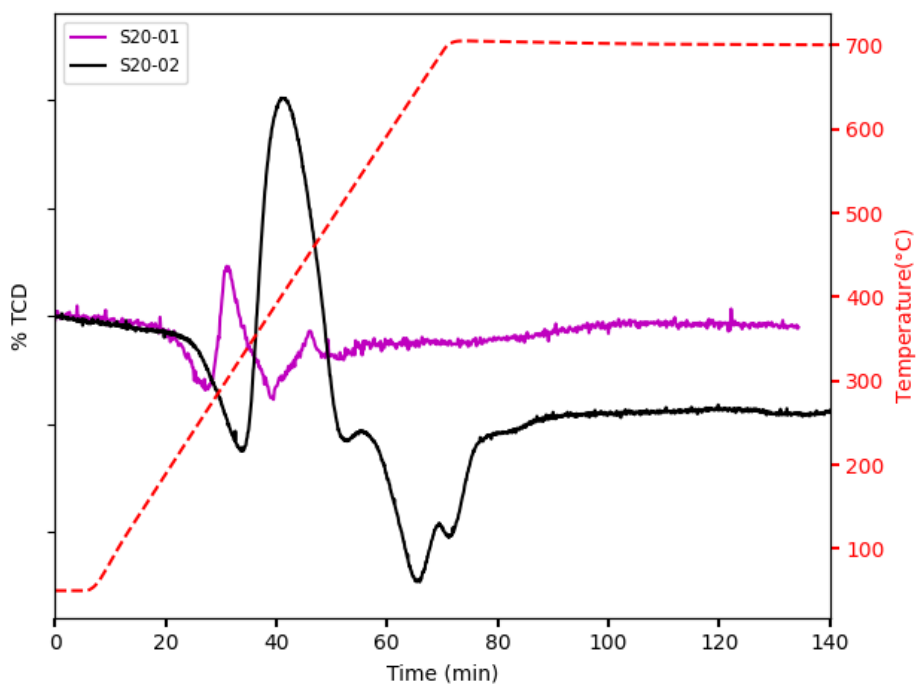


Figure B.2: CO_2 TCD signal and temperature versus time during TPO experiment for two S20 parallels.

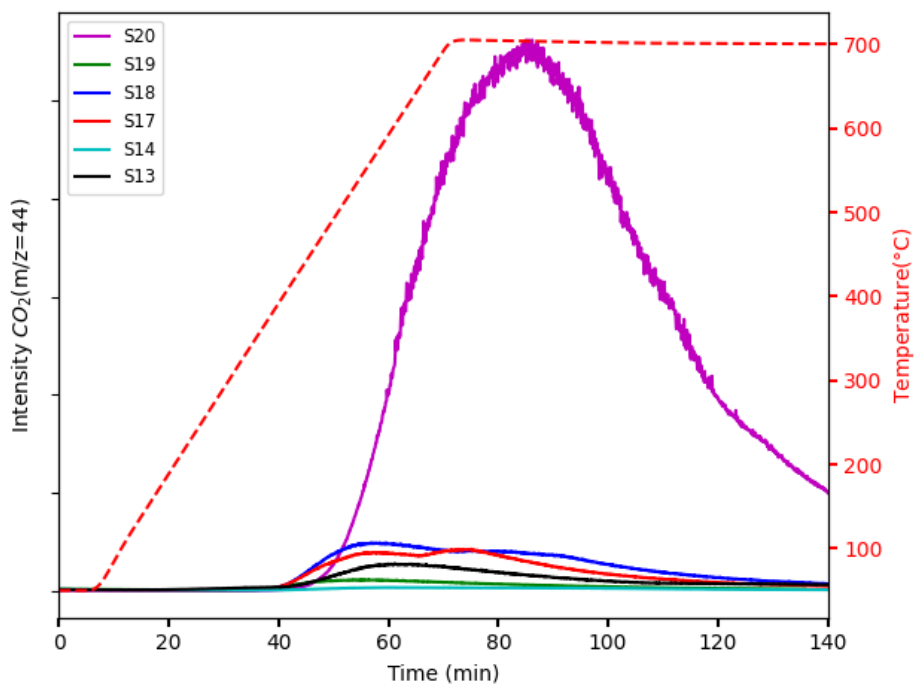


Figure B.3: CO_2 MS signal ($m/z=44$) and temperature versus time during TPO experiment for all reacted contact mass samples.

C Full TPO Procedure

Starting Conditions	Treatment Gas	Argon
	Flow Through Saturator? Y/N.....	<input type="checkbox"/> No
	Saturator Temperature, 25-75 degC..	25 degC
	Flow Rate, 5-50 cc/min	50 cc/min
	Initial Temperature, 25 -1100 degC	30 degC
	Hold Time, 0-999 min	10 min
Blending	Blend Gases?.....	<input type="checkbox"/> No
	Blend Gas.....	No Gas Selected
	Flow Rate, 5-50 cc/min.....	0.0 cc/min
	Carrier Gas	No Gas Selected
	Flow Rate, 5-50 cc/min	0 cc/min
	Auxiliary Gas.....	No Gas Selected
	Flow Rate, 0.4-4 cc/min.....	0 cc/min
Ramp & Hold #1	Perform This Step? Y/N.....	<input checked="" type="checkbox"/> Yes
	Setpoint Temperature, 25 -1100 degC..	105 degC
	Ramp Rate, +30-30 degC/min.....	10.00 degC/min
	Hold Time, 0-999 min.....	10 min
Ramp & Hold #2	Perform This Step? Y/N.....	<input checked="" type="checkbox"/> Yes
	Setpoint Temperature, 25 -1100degC..	55 degC
	Ramp Rate, +30-30 degC/min.....	10.00 degC/min
	Hold Time, 0-999 min.....	2 min
Postflush	Flow Rate, 5- 50 cc/min	30 cc/min
	Hold Time, 0-999 min.....	5 min
Ending Conditions:	Abort WatchDog.....	04:00:00 Hr:Mn:Sec (or Inf)

Accept
Step# 1
Treatment
05:30:07 PM
06/05/2021
Cancel

Figure C.4: Detailed settings for TPO procedure step 1, pretreatment.

Detector	Disable TCD? Y/N.....	<input type="checkbox"/> No
	Delay for Auto Baseline? Y/N.....	<input type="checkbox"/> Yes
	TCD Current, 50-200 mA.....	▲ 110 mA
	TCD Gain, 1-100.....	▲ 2
Starting Conditions	Signal Sample Rate, 0.1-100 sec/pt...	▲ 5.0 sec/pt
	Carrier Gas	5% O2/He
	Flow Rate, 5-50 cc/min	▲ 50 cc/min
	Initial Temperature, 25 -1100 degC	▲ 50 degC
	Hold Time, 0-999 min	▲ 5 min
Blend Conditions	Blend Gases? Y/N.....	<input type="checkbox"/> No
	Blend Gas.....	No Gas Selected
	Flow Rate, 5-50 cc/min.....	▲ 0.0 cc/min
	Treatment Gas	No Gas Selected
	Flow Rate, 5-50 cc/min	▲ 0
	Auxiliary Gas.....	No Gas Selected
Ramp & Hold	Flow Rate, 0.4-4 cc/min.....	▲ 0
	End Temperature, 25 -1100 degC.....	▲ 700 degC
	Ramp Rate, +30-30 degC/min.....	▲ 10.00 degC/min
	Hold Time, 0-999 min.....	▲ 80 min
Postflush	Flow Rate, 5-50 cc/min	▲ 25 cc/min
	Hold Time, 0-999 min.....	▲ 5 min
Ending Conditions:	Abort WatchDog.....	▲ 07:00:00 Hr:Mn:Sec (or Inf)

Accept
Step# 2
TPR/TPO
05:31:30 PM
06/05/2021
Cancel

Figure C.5: Detailed settings for TPO procedure step 2, TPO.

Starting Conditions	Treatment Gas	Argon
	Flow Through Saturator? Y/N.....	<input type="checkbox"/> No
	Saturator Temperature, 25-75 degC..	▲ 25 degC
	Flow Rate, 5-50 cc/min	▲ 50 cc/min
	Initial Temperature, 25-1100 degC	▲ 700 degC
	Hold Time, 0-999 min	▲ 5 min
Blending	Blend Gases?.....	<input type="checkbox"/> No
	Blend Gas.....	No Gas Selected
	Flow Rate, 5-50 cc/min.....	▲ 0.0 cc/min
	Carrier Gas	No Gas Selected
	Flow Rate, 5-50 cc/min	▲ 0 cc/min
	Auxiliary Gas.....	No Gas Selected
	Flow Rate, 0.4-4 cc/min.....	▲ 0 cc/min
Ramp & Hold #1	Perform This Step? Y/N.....	<input type="checkbox"/> Yes
	Setpoint Temperature, 25-1100 degC.	▲ 50 degC
	Ramp Rate, +30-30 degC/min.....	▲ 30.00 degC/min
	Hold Time, 0-999 min.....	▲ 10 min
Ramp & Hold #2	Perform This Step? Y/N.....	<input type="checkbox"/> No
	Setpoint Temperature, 25-1100degC.	▲ 25 degC
	Ramp Rate, +30-30 degC/min.....	▲ 5.00 degC/min
	Hold Time, 0-999 min.....	▲ 15 min
Postflush	Flow Rate, 5- 50 cc/min	▲ 25 cc/min
	Hold Time, 0-999 min.....	▲ 5 min
Ending Conditions:	Abort WatchDog.....	▲ 04:00:00 Hr:Mn:Sec (or Inf)

Accept
 Step# 3
 Treatment
 05:32:17 PM
 06/05/2021
Cancel

Figure C.6: Detailed settings for TPO procedure step 3, posttreatment.

D Risk Assessment



ID	40040	Status	Date
Risk Area	Risikovurdering: Helse, miljø og sikkerhet (HMS)	Created	02.09.2020
Created by	Lasse Svendsen Chrobak	Assessment started	08.09.2020
Responsible	Lasse Svendsen Chrobak	Measures decided	
		Closed	

Risk Assessment:
CAT, Master Student, 2021, Lasse Svendsen Chrobak

Valid from-to date:

9/2/2020 - 9/2/2023

Location:

Gløshaugen, Kjemiblokk 5 (K5)

Goal / purpose

Risk assessment for my specialization project and Master's thesis: "Characterization of Coke Formation in The direct Synthesis of Dimethylchlorosilane – collaboration with Elkem – Bluestar"

Characterization of silicon sample from Elkem used in the production of methylchlorosilanes (used for the production of silicone products, and also the characterization of their corresponding catalysts and carbon deposited on them.
- Different techniques such as AES, XRD, S(T)EM, Raman, FT-IR, TGA, and TPO.

Background

Specialization project/Master's student

The characterization techniques mentioned above will be used in this project. The samples used in the characterization techniques is reacted and unreacted contact mass samples containing mainly Is, some Cu, and traces of Zn, Sn, Al, C, O elements. The samples will mainly be characterized in the form of powder, but for FTIR a liquid extracted sample will also be analyzed.

Description and limitations

The samples used in the characterization techniques is reacted and unreacted contact mass samples containing mainly Is, some Cu, and traces of Zn, Sn, Al, C, O elements. The samples will mainly be characterized in the form of powder, but for FTIR a liquid extracted sample will also be analyzed.

Characterization techniques:

- Thermogravimetric analysis (TGA) to study and analyze mass change with temperature. The samples will be heated in the range 30 to 800 °C with. Using synthetic air and protective argon gases at atmospheric pressure for a duration of almost 3 hours per run.
 - Raman Spectroscopy (and micro Raman) to determine the degree of order of the carbon species present in the samples. Ex-situ experiment using 633 nm visible laser.
 - FT-IR to identify the functional groups in the contact mass samples, and observe chemical properties. samples will be analyzed in both powder and liquid forms under this equipment.
 - XRD analysis to determine the the crystalline structure of the samples.
 - ST(EM) (and SEM) and AES (Nanolab cleanroom): will be used to characterize the nanoscale structure of our samples and to have proper insights into their properties and their elemental distributions.
- TPO will be used to analyze the mass change

Safety measures to prevent spread of COVID-19:

- Avoid touching the face
- Disinfection of all surfaces you are in contact with, with ethanol or soap water.
- Use nitrile gloves for shared lab set-ups
- Keep at least 1 meter distance from colleagues.
- Using Microsoft Teams to book labs and track who uses the lab.

Prerequisites, assumptions and simplifications

Norges teknisk-naturvitenskapelige universitet (NTNU)	Print date:	Printed by:	Page:
Unntatt offentlighet jf. Offentlighetsloven § 14	24.06.2021	Lasse Svendsen Chrobak	1/14



-
- HSE training
 - Training for XRD (K2 113)
 - Training for TGA (lab K5 441)
 - Training for Raman spectroscopy (lab K5 427)
 - Training for FT-IR (lab K5-310)
 - Training for TPO (Hall D, 2.6)
 - Training for S(T)EM (NanoLab cleanroom)
 - Training for AES (NanoLab)
 - Training for Micro Raman spectroscopy (NanoLab cleanroom)

Attachments

[Ingen registreringer]











References

[Ingen registreringer]







Summary, result and final evaluation

The summary presents an overview of hazards and incidents, in addition to risk result for each consequence area.

Hazard:	Usage of chemicals			
Incident:	Contact with silicon powder and samples provided by Elkem			
Consequence area:	Helsete Ytre miljø	Risk before measures: Risk before measures:	 Risiko after measures:  Risiko after measures:	 
Hazard:	X-ray exposure in the XRD lab			
Incident:	Skin burn from X-ray exposure			
Consequence area:	Helsete	Risk before measures:	 Risiko after measures:	
Hazard:	Using the labs during the COVID-19 pandemic			
Incident:	Not to be analyzed.			
Hazard:	High temperature of up to 800 °C in TGA (lab K5 441)/TPO(IHall D 2.6)			
Incident:	Hand burn			
Consequence area:	Helsete	Risk before measures:	 Risiko after measures:	
Hazard:	Laser class 3 in Raman spectroscopy(lab K5 427)			
Incident:	Eye injury			
Consequence area:	Helsete	Risk before measures:	 Risiko after measures:	



Hazard:	Pressurized gas in characterization labs			
Incident:	Gas leak			
Consequence area:	Helse	Risk before measures:	 Risiko after measures:	
	Materielle verdier	Risk before measures:	 Risiko after measures:	

Final evaluation



Organizational units and people involved

A risk assessment may apply to one or more organizational units, and involve several people. These are listed below.

Organizational units which this risk assessment applies to

- Institutt for kjemisk prosesseteknologi

Participants

Mehdi Mahmoodinia
Hilde Johnsen Venvik

Readers

Estelle Marie M. Vanhaecke
Anne Hoff
Karin Wiggen Dragsten
Samuel K. Regli
Jens Norrman

Others involved/stakeholders

[Ingen registreringer]

The following accept criteria have been decided for the risk area Risikovurdering: Helse, miljø og sikkerhet (HMS):





Overview of existing relevant measures which have been taken into account

The table below presents existing measures which have been taken into account when assessing the likelihood and consequence of relevant incidents.

Hazard	Incident	Measures taken into account
Usage of chemicals	Contact with silicon powder and samples provided by Elkem	Safety goggles
	Contact with silicon powder and samples provided by Elkem	Lab gloves
	Contact with silicon powder and samples provided by Elkem	Lab coat
X-ray exposure in the XRD lab	Skin burn from X-ray exposure	Safety goggles
	Skin burn from X-ray exposure	Lab gloves
High temperature of up to 800 °C in TGA (lab K5 441)/TPO(Hall D 2.6)	Hand burn	Safety goggles
	Hand burn	Lab gloves
Laser class 3 in Raman spectroscopy(lab K5 427)	Eye injury	Safety goggles
Pressurized gas in characterization labs	Gas leak	Gas detectors

Existing relevant measures with descriptions:

Safety goggles

[Ingen registreringer]

Lab gloves

[Ingen registreringer]

Gas detectors

[Ingen registreringer]

Lab coat

[Ingen registreringer]

Disinfection with ethanol

[Ingen registreringer]



Risk analysis with evaluation of likelihood and consequence

This part of the report presents detailed documentation of hazards, incidents and causes which have been evaluated. A summary of hazards and associated incidents is listed at the beginning.

The following hazards and incidents has been evaluated in this risk assessment:

- **Usage of chemicals**
 - Contact with silicon powder and samples provided by Elkem
- **X-ray exposure in the XRD lab**
 - Skin burn from X-ray exposure
- **High temperature of up to 800 °C in TGA (lab K5 441)/TPO(IHall D 2.6)**
 - Hand burn
- **Laser class 3 in Raman spectroscopy(lab K5 427)**
 - Eye injury
- **Pressurized gas in characterization labs**
 - Gas leak



Detailed view of hazards and incidents:

Hazard: Usage of chemicals

Incident: Contact with silicon powder and samples provided by Elkem

.....

Cause: Improper handling

Likelihood of the incident (common to all consequence areas): **Less likely (2)**

Kommentar:

Usage of nitrile gloves and goggles are mandatory inside the labs.

Consequence area: Helse

Assessed consequence: **Medium (2)**

Comment: Contact with silicon may lead to reddening of skin. Usage of lab coat, goggles and nitrile gloves makes the consequence moderate.

Risk:



Consequence area: Ytre miljø

Assessed consequence: **Small (1)**

Comment: Careful handling of the silicon powder will make the chance of any incident minimal.

Risk:





Hazard: X-ray exposure in the XRD lab

Incident: Skin burn from X-ray exposure

.....

Cause: Cracks in the glass

Likelihood of the incident (common to all consequence areas): **Less likely (2)**

Kommentar:

Lab training is provided and safety goggles and lab gloves are mandatory. The XRD machine is only used by special trained personnel.

Consequence area: Helse

Assessed consequence: **Medium (2)**

Comment: Exposure to X-rays may cause skin burn.

Risk:





Hazard: High temperature of up to 800 °C in TGA (lab K5 441)/TPO(IHall D 2.6)

Incident: Hand burn

.....

Cause: Direct contact

Likelihood of the incident (common to all consequence areas): **Unlikely (1)**

Kommentar:

There is highly unlikely to get direct contact with the sample crucible before TGA has cooled down.

Consequence area: Helse

Assessed consequence: **Very large (4)**

Comment: Direct contact with the crucible at 800 °C can cause serious skin damage. Proper handling and adequate knowledge of the equipment must be employed.

Risk:





Hazard: Laser class 3 in Raman spectroscopy(lab K5 427)

Incident: Eye injury

.....

Cause: Direct contact with laser

Likelihood of the incident (common to all consequence areas): **Unlikely (1)**

Kommentar:

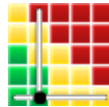
Knowledge and training of Raman/IR and the use of PPE en the form of safety goggles reduces the likelihood.

Consequence area: Helse

Assessed consequence: **Medium (2)**

Comment: Exposure to class 3 laser is considered less dangerous when using proper PPE (goggles).

Risk:





Hazard: Pressurized gas in characterization labs

Incident: Gas leak

.....

Cause: Improper installation

Likelihood of the incident (common to all consequence areas): **Less likely (2)**

Kommentar:

All characterization areas are equipped with proper detectors and in case of a gas leak, it will be detected by gas detectors.

Consequence area: Helse

Assessed consequence: **Small (1)**

Comment: Synthetic air or an inert gas like Ar is not readily harmful.

Risk:



Consequence area: Materielle verdier

Assessed consequence: **Medium (2)**

Comment: Leakage of gas over time can be expensive, but the leakage can be detected in time using gas detectors.

Risk:





Overview of risk mitigating measures which have been decided:

Below is an overview of risk mitigating measures, which are intended to contribute towards minimizing the likelihood and/or consequence of incidents:

Overview of risk mitigating measures which have been decided, with description:



Detailed view of assessed risk for each hazard/incident before and after mitigating measures

